# Healing capillary films

**Zhong Zheng**[1,2]†, **Marco A. Fontelos**[3]‡, **Sangwoo Shin**[1,4],
**Michael C. Dallaston**[5], **Dmitri Tseluiko**[6],
**Serafim Kalliadasis**[5], AND **Howard A. Stone**[1]

[1]Department of Mechanical and Aerospace Engineering,
Princeton University, Princeton, New Jersey 08544, USA
[2]Department of Applied Mathematics and Theoretical Physics,
University of Cambridge, Cambridge CB3 0EZ, UK
[3]Instituto de Ciencias Matemáticas, C/Nicolás Cabrera, Madrid, 28049, ESP
[4]Department of Mechanical Engineering, University of Hawaii at Manoa,
Honolulu, Hawaii 96822, USA
[5]Department of Chemical Engineering, Imperial College London,
London SW7 2AZ, UK
[6]Department of Mathematical Sciences, Loughborough University,
Loughborough LE11 3TU, UK

Consider the dynamics of a healing film driven by surface tension, that is, the inward spreading process of a liquid film to fill a hole. The film is modelled using the lubrication (or thin-film) approximation, which results in a fourth-order nonlinear partial differential equation. We obtain a self-similar solution describing the early-time relaxation of an initial step-function condition and a family of self-similar solutions governing the finite-time healing. The similarity exponent of this family of solutions is not determined purely from scaling arguments; instead, the scaling exponent is a function of the finite thickness of the prewetting film, which we determine numerically. Thus, the solutions that govern the finite-time healing are self-similar solutions of the second kind. Laboratory experiments and time-dependent computations of the partial differential equation are also performed. We compare the self-similar profiles and exponents with both measurements in experiments and time-dependent computations near the healing time, and we observe good agreement in each case.

---

## 1. Introduction

By "healing" of a thin viscous film we refer to the inward spreading of a film to fill a hole or dry spot in the film (see figure 1). Healing films are ubiquitous in a wide spectrum of natural phenomena and technological applications from interaction of plant leaves with rain water to self-healing, spin coating, and glass transition processes (see, e.g., Backholm *et al.* 2014; Blossey 2003; Dijksman *et al.* 2015; Herminghaus *et al.* 2008), and the dynamics of axisymmetric holes or dry spots in thin films has been studied extensively from a modelling perspective.

In previous studies, a major focus has been on the stability of holes of certain size, which is dependent on the relative importance of surface tension, buoyancy (gravity), and

† Emails: zzheng@alumnni.princeton.edu, marco.fontelos@icmat.es, hastone@princeton.edu.
‡ Z. Zheng and M. A. Fontelos contributed equally to this work.

contact line effects (e.g., surface wettability). Moriarty & Schwartz (1993) used a lubrication model to investigate the stability and evolution of holes. While, for a non-wetting surface, there may exist an equilibrium hole configuration (Padday 1971). This situation is unstable (Taylor & Michael 1973; Sharma & Ruckenstein 1990), and the hole will either heal, or expand: either indefinitely, or, in the presence of an outer boundary, until the fluid is collected in a ring near that boundary. In the work of Moriarty & Schwartz (1993), advancing and retreating contact angles were prescribed, and the contact line was moved artificially by a mesh point if the angle was greater or less than the advancing or retreating value, respectively (effectively a kind of numerical slip). The stability was also studied by López *et al.* (2001), using the lubrication approximation together with a more natural Navier slip model (along with an assumed contact angle–velocity relation) to regularize the contact line singularity, instead of the numerical slip that Moriarty & Schwartz (1993) implemented, and the numerical results compared favourably to subsequent experimental work (Bankoff *et al.* 2003).

In the present study, our particular focus is on the thickness profile and contact line position as a hole heals (see, e.g., Diez *et al.* 1992; López *et al.* 2001; Zheng *et al.* 2014; Dijksman *et al.* 2015). In this regard, López *et al.* (2001) adopted a quasi-static approximation, i.e., that the contact line velocity is much smaller than the time for the thickness profile to reach the quasi-steady balance between gravity and surface tension. Their results compared well with the experiments of Diez *et al.* (1992), which were performed in a gravity-dominated parameter regime. In fact, quasi-steadiness is a common assumption in the modelling of spreading droplets and films (Hocking 1983; Savva & Kalliadasis 2009); however, in the limit of a healing hole, the velocity is (theoretically) unbounded at the time the hole closes, so there is no longer a clear separation of these time scales. We expect this to be particularly true for healing films driven primarily by capillarity, rather than gravity, as the curvature becomes infinite as the hole eventually closes. Thus, instead of modelling the hole-healing dynamics as a quasi-steady process (see, e.g., Bostwick *et al.* 2017), we employ an alternate approach, and assume self-similarity in the thickness profile in this study.

We note that self-similar healing films have been studied previously for the case when the flow is driven purely by gravity (Gratton & Minotti 1990; Diez *et al.* 1992), in which a second-order nonlinear diffusion equation describes the time evolution of the interface shape. Also, the gravity-driven healing is analogous to the converging flow processes in a porous medium (or, a Hele-Shaw cell) with horizontal heterogeneity (Zheng *et al.* 2014), and the fluid loss effect can be included for healing above a permeable substrate (Zheng *et al.* 2015). Although common flows of spreading thin films often admit similarity solutions where the scaling exponents can be identified by dimensional arguments (self-similarity of the first kind), the healing dynamics for a gravity current admits a similarity solution where the scaling exponent is determined from the solution of a nonlinear eigenvalue problem (self-similarity of the second kind) (Barenblatt 1979).

For the case of surface-tension-driven flows, as in the present study, the evolution of the interface shape is described by a fourth-order nonlinear partial differential equation (PDE) of the evolution type, that may behave very differently from the nonlinear diffusion equation for gravity-driven flows (see, e.g., Voinov 1976; Tanner 1979; Hocking 1983; de Gennes *et al.* 1990; Jensen 1994; Oron *et al.* 1997; Kalliadasis *et al.* 2000; Craster & Matar 2009; Snoeijer & Andreotti 2013; Eggers & Fontelos 2015). Here we seek various self-similar solutions for this fourth-order PDE and support our findings via numerical simulations and experiments. We start in § 2 by introducing the theoretical model and deriving the self-similar solutions that develop at different times. In § 3, we report on detailed laboratory-scale experiments for conditions where surface-tension-driven spreading
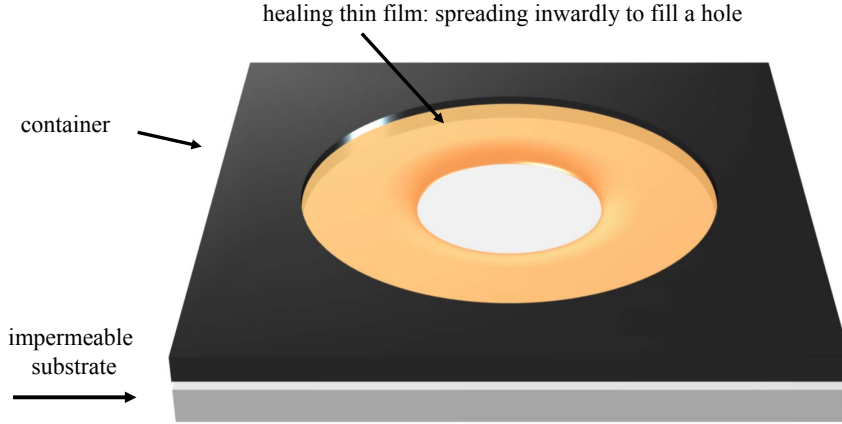
FIGURE 1. Schematic of the healing of a thin film, i.e. the inward spreading of a liquid film to fill a "hole" at the centre. Here we focus in the regime when the flow of the thin liquid film is driven by surface tension.

dominates the dynamics. We then compare the theoretical predictions and experimental observations for the front location and the interface shape. In § 4, we present numerical simulations of the original PDE and compare the results with the self-similar solutions. We close the manuscript in § 5 by summarizing the major findings of this work.

## 2. Theoretical model

### 2.1. *Governing equations*

We consider a converging thin-film flow driven by surface tension and assume an axisymmetric geometry, as depicted in figure 2. We assume that the liquid domain is long and thin, and the flow is radial (one–dimensional), so that the lubrication approximation holds. We use $\tilde{t}$, $\tilde{r}$, $\mu$ and $\gamma$ to denote time, the radial coordinate, the viscosity of the fluid, and surface tension coefficient between air and the spreading fluid, respectively. We also assume that the spreading fluid perfectly wets the substrate so that the contact angle vanishes. Stipulating radial symmetry and neglecting gravitational effects, the governing partial differential equation (PDE) for the interface shape $\tilde{h}\left(\tilde{r},\tilde{t}\right)$ is (e.g. Oron *et al.* 1997; Bonn *et al.* 2009)

$$\frac{\partial \tilde{h}}{\partial \tilde{t}} + \frac{\gamma}{3\mu} \frac{1}{\tilde{r}} \frac{\partial}{\partial \tilde{r}} \left( \tilde{r}\tilde{h}^3 \frac{\partial}{\partial \tilde{r}} \left( \frac{1}{\tilde{r}} \frac{\partial}{\partial \tilde{r}} \left( \tilde{r}\frac{\partial \tilde{h}}{\partial \tilde{r}} \right) \right) \right) = 0. \tag{2.1}$$

A further assumption is that initially viscous fluid of height $\tilde{h}_0$ fills the gap between $\tilde{r}_0$, the location of a lock gate, and $\tilde{r}_{\mathrm{out}}$, the location of a stationary outer boundary. Within the lock gate there is a thin layer of a prewetting liquid film of thickness $\tilde{h}_{\mathrm{pw}}$. The introduction of a prewetting film is consistent with our lock-release experiments, as described in § 3, and is also consistent with other converging flow situations generated from an instantaneous stop of a rotating container (Dijksman *et al.* 2015). In addition, the existence of a prewetting film regularises the stress singularity at the front. Thus, the
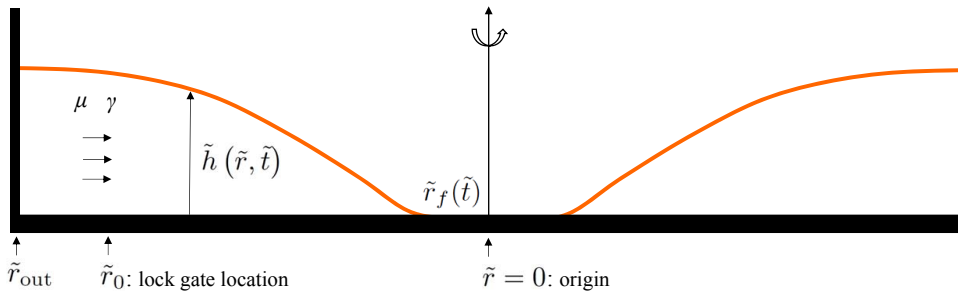
FIGURE 2. A healing capillary film: a converging thin viscous film is driven by surface tension. The film thickness is denoted by $\tilde{h}(\tilde{r}, \tilde{t})$, while the location of the propagating front is denoted by $\tilde{r}_f(\tilde{t})$. $\tilde{r}_0$ represents the location of a lock gate and $\tilde{r}_{\text{out}}$ the location of the outer boundary. The viscosity of the fluid and surface tension coefficient are denoted by $\mu$ and $\gamma$, respectively.

initial condition takes the form of

$$\tilde{h}(\tilde{r}, 0) = \begin{cases} \tilde{h}_0, & \tilde{r}_0 \leqslant \tilde{r} \leqslant \tilde{r}_{\text{out}}, \\ \tilde{h}_{\text{pw}}, & 0 \leqslant \tilde{r} < \tilde{r}_0, \end{cases} \tag{2.2}$$

and we are interested in the dynamics of spreading toward the origin ($\tilde{r} = 0$). This step initial condition is consistent with our lock-release experiments. We also note that, although the thin-film model equation is strictly speaking valid for small interfacial slopes and is expected to break down when interfacial slopes are large, the step initial condition is rapidly smoothed out to a shape that is appropriate for the thin-film approximation (see, e.g., Huppert & Woods 1995; McGraw *et al.* 2012).

To close the problem, we impose the following boundary conditions:

$$\frac{\partial \tilde{h}}{\partial \tilde{r}} = \frac{\partial^3 \tilde{h}}{\partial \tilde{r}^3} = 0 \text{ at } \tilde{r} = 0, \text{ and } \frac{\partial \tilde{h}}{\partial \tilde{r}} = \frac{\partial}{\partial \tilde{r}} \left( \frac{1}{\tilde{r}} \frac{\partial}{\partial \tilde{r}} \left( \tilde{r} \frac{\partial \tilde{h}}{\partial \tilde{r}} \right) \right) = 0 \text{ at } \tilde{r} = \tilde{r}_{\text{out}}. \tag{2.3}$$

The first pair of these are symmetry conditions applied at the centre of the domain, while the second pair are, respectively, 90° contact angle and zero-flux conditions at the outer wall (see, e.g., López *et al.* 2001, for a discussion of the outer contact-angle condition).

Next, we define dimensionless variables $h \equiv \tilde{h}/\tilde{h}_0$, $r \equiv \tilde{r}/\tilde{r}_0$ and $t \equiv \tilde{t}/\tilde{t}_c$, where the characteristic time is chosen as

$$\tilde{t}_c = \frac{3\mu \tilde{r}_0^4}{\gamma \tilde{h}_0^3}, \tag{2.4}$$

and obtain the dimensionless form of equation (2.1):

$$\frac{\partial h}{\partial t} + \frac{1}{r} \frac{\partial}{\partial r} \left( r h^3 \frac{\partial}{\partial r} \left( \frac{1}{r} \frac{\partial}{\partial r} \left( r \frac{\partial h}{\partial r} \right) \right) \right) = 0. \tag{2.5}$$

The dimensionless initial condition (2.2) becomes

$$h(r, 0) = \begin{cases} 1, & 1 \leqslant r \leqslant r_{\text{out}}, \\ h_{\text{pw}}, & 0 \leqslant r < 1, \end{cases} \tag{2.6}$$

where $h_{\text{pw}} \equiv \tilde{h}_{\text{pw}}/\tilde{h}_0 \ll 1$ and $r_{\text{out}} \equiv \tilde{r}_{\text{out}}/\tilde{r}_0 \gg 1$, and the dimensionless boundary

conditions (2.3) become

$$\frac{\partial h}{\partial r} = \frac{\partial^3 h}{\partial r^3} = 0 \text{ at } r = 0, \text{ and } \frac{\partial h}{\partial r} = \frac{\partial}{\partial r}\left(\frac{1}{r}\frac{\partial}{\partial r}\left(r\frac{\partial h}{\partial r}\right)\right) = 0 \text{ at } r = r_{\text{out}}. \qquad (2.7)$$

Equation (2.5) can be solved subject to the initial and boundary conditions (2.6), (2.7) and provides the time evolution of the profile shape $h(r, t)$.

While the main focus of this study is on the behaviour of the film close to the time when it heals, it is also interesting to analyse the early-time relaxation process. We provide a self-similar solution in Appendix A for the early-time relaxation dynamics from the initial step condition (2.6).

## 2.2. *Similarity transform*

We now focus on the late-time dynamics as the hole closes, i.e. as $r_f(t) \to 0$. We use $t_0$ to denote the dimensionless healing time, that is, the time for the (circular) front of the air-fluid interface to reach the origin ($r = 0$), and we look for a self-similar solution for equation (2.5) of the form

$$h(r, t) = (t_0 - t)^\alpha f(\xi), \quad \text{where} \quad \xi \equiv \frac{r}{(t_0 - t)^\beta}. \qquad (2.8)$$

From dimensional analysis and (2.5), we obtain the following relationship between the exponents

$$\alpha = \frac{(4\beta - 1)}{3}. \qquad (2.9)$$

We can then rewrite equation (2.5) as an ordinary differential equation (ODE):

$$-\frac{(4\beta - 1)}{3}f + \beta\xi\frac{\mathrm{d}f}{\mathrm{d}\xi} + \frac{1}{\xi}\frac{\mathrm{d}}{\mathrm{d}\xi}\left(\xi f^3\frac{\mathrm{d}}{\mathrm{d}\xi}\left(\frac{1}{\xi}\frac{\mathrm{d}}{\mathrm{d}\xi}\left(\xi\frac{\mathrm{d}f}{\mathrm{d}\xi}\right)\right)\right) = 0, \qquad (2.10)$$

where the exponent $\beta$ is as yet undetermined.

### 2.2.1. *Far-field condition*

Appropriate boundary conditions are needed to solve equation (2.10) for the interface shape $f(\xi)$ and determine parameter $\beta$. The similarity solution will not hold everywhere in $r$ and $t$, but rather, in a region near the apparent contact line, for time sufficiently close to $t_0$. Since $\xi \to \infty$ for fixed $r$ as $t \to 0$, the similarity solution is defined on the semi-infinite domain $0 < \xi < \infty$.

The rate of change of film thickness $\partial h/\partial t$ blows up as $(t_0 - t)^{\alpha-1}$. However, we expect $\partial h/\partial t$ to remain bounded away from the middle of the hole, which requires the first two terms in (2.10) to balance. This gives the far-field "quasi-stationarity" condition

$$-\frac{(4\beta - 1)}{3}f + \beta\xi\frac{\mathrm{d}f}{\mathrm{d}\xi} \to 0 \quad \text{as} \quad \xi \to \infty. \qquad (2.11)$$

Solving this equation provides

$$f(\xi) \sim a_1\xi^{(4\beta-1)/(3\beta)} \quad \text{as} \quad \xi \to \infty. \qquad (2.12)$$

This kind of condition has been employed previously in studying other problems involving the formation of finite-time singularities such as the capillary-driven breakup of viscous threads (see, e.g., Eggers 1993; Papageorgiou 1995; Brenner *et al.* 1996; Lister & Stone 1998; Eggers & Fontelos 2009), and the van der Waals-driven rupture of thin films (see, e.g., Zhang & Lister 1999; Witelski & Bernoff 1999; Dallaston *et al.* 2017).

### 2.2.2. *Near-field condition*

ODE (2.10) permits a number of different near-field behaviours, as either $\xi$ or $f$ approaches zero. However, only particular solutions will exhibit behaviour that can be matched to a prewetting film. Assume that $f$ becomes small at an apparent contact line $\xi = \xi_0 > 0$, while $f' \equiv \mathrm{d}f/\mathrm{d}\xi$ remains of order unity: the dominant terms in (2.10) in an 'inner region' near the contact line are $\beta\xi_0 f' + (f^3 f''')' = 0$, which can be integrated once to give

$$\beta\xi_0 f + f^3 \frac{\mathrm{d}^3 f}{\mathrm{d}\xi^3} = \epsilon. \tag{2.13}$$

If $f$ goes to zero it must do so as $f \sim c_1(\xi - \xi_0)^{3/4}$, which is unphysical and cannot match to a thin prewetting film. However, (2.13) also has solutions with a thin prewetting film $f \sim f_{\mathrm{pw}} = \epsilon/(\beta\xi_0) > 0$ for $\xi \ll \xi_0$ (Landau & Levich 1942; Myers 1998). We will find below that there is only one such solution to (2.10) that has such a film for any given $\beta$, once certain scale invariances have been accounted for. An expanded account on all the possible near-field behaviours is presented in Appendix C.3.

### 2.3. *Self-similar solutions for general exponent $\beta$*

#### 2.3.1. *Shooting procedure*

To compute the self-similar solutions for ODE (2.10), a shooting procedure can be used from a large value of $\xi$, representing the far field, toward the contact line. For example, when $\beta = 2/5$, the far-field behaviour of $f(\xi)$ has a relatively simple form (with details provided in Appendix B)

$$f(\xi) \sim a_1 \xi^{1/2} + a_2 \xi^{-8/5} \mathrm{e}^{-6/5(2/5)^{1/3} a_1^{-1} \xi^{5/6}} + O(1) \quad \text{as} \quad \xi \to \infty, \tag{2.14}$$

where $a_1$ and $a_2$ are two free parameters. Thus, by specifying the values of $a_1$ and $a_2$, we can obtain the values of $f$ and its derivatives at a far-field location that can be used in the shooting procedure. Note, however, that since (2.10) is invariant under the transformation $f \mapsto \lambda f$, $\xi \mapsto \lambda^{3/4}\xi$, where $\lambda$ is a positive constant, we may set $a_1 = 1$ without loss of generality, and, by varying $a_2$, construct the one-parameter family of solutions that are unique up to such a rescaling.

In figure 3, we show representative solutions of (2.10) for $\beta = 2/5$, computed using the described shooting procedure. In all the cases, we start from a far-field location $\xi_\infty = 10$, and shoot toward the origin using the MATLAB subroutine ODE45. Initial conditions are provided by setting $a_1 = 1$ and varying the values of $a_2$ from $-10$ to $10$. From figure 3, we observe five distinct near-field behaviours as $a_2$ varies: blow-up, generic touch-down, touch-down at the origin, a thick film, and a non-generic solution that separates the generic touch-down solutions from the blow-up ones. It is this non-generic solution that has the appropriate structure near an apparent contact line, as we see next.

#### 2.3.2. *Alternative procedures*

In principle, we can compute numerical solutions to ODE (2.10) for a range of $\beta$ values, and vary $a_1$ to find the critical solution between blow-up and touch-down. For $\beta \neq 2/5$, however, there is an infinite series of algebraic terms in the far-field behaviour, and so it is much harder to set the prefactor on the exponential, e.g., $a_2$ in (2.14), numerically. As an alternative, we handle the far field for general $\beta$ by posing a suitable boundary-value problem on the interval $[\xi_\infty/2, \xi_\infty]$, where $\xi_\infty \gg 1$ represents a far-field location, and then solving an initial-value problem on $[0, \xi_\infty/2]$ from $\xi = \xi_\infty/2$ toward $\xi = 0$ (the origin). In particular, the following conditions are employed for the boundary-value
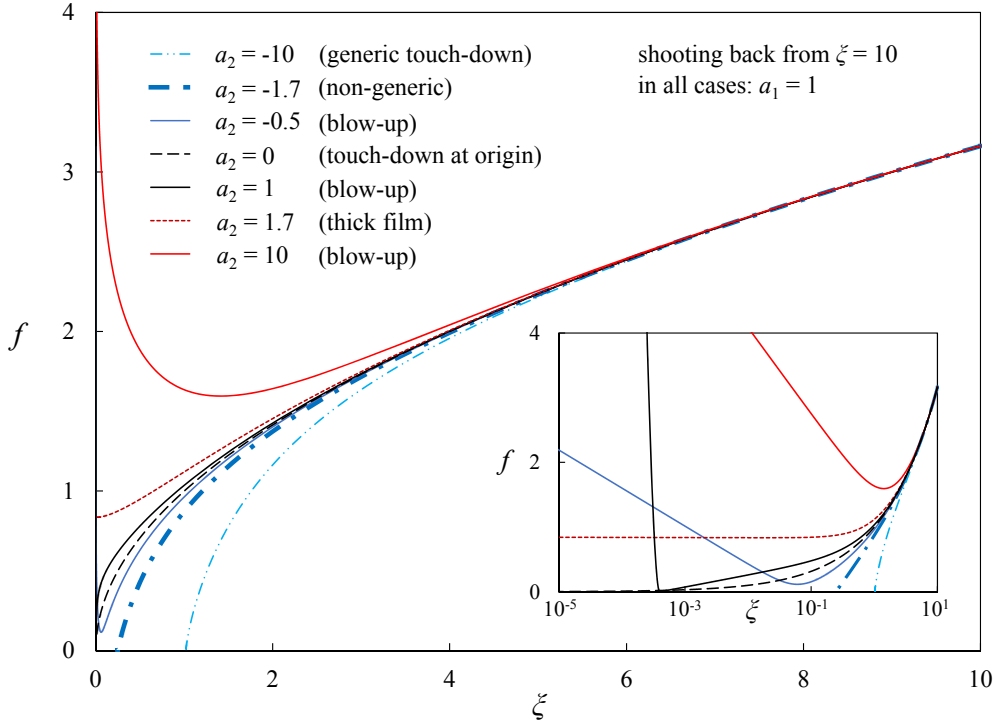
FIGURE 3. Representative solutions of (2.10) with similarity exponent $\beta = 2/5$ using a shooting procedure from a far-field location. In all cases, $a_1 = 1$ and the far-field location is chosen as $\xi_\infty = 10$. Consistent with the asymptotic analysis for the near-field behaviour, five different scenarios have been observed as is indicated in the legend: blow-up, generic touch-down, touch–down at the origin, a thick film, and a non-generic critical solution that represents the crossover between generic touch-down and blow-up solutions (see Appendix C for details). The inset is a semi-log plot of the figure, which highlights the near-field behaviours. The non-generic solution corresponds to the interface shape of the healing capillary film problem.

problem on $[\xi_\infty/2, \; \xi_\infty]$:

$$-\frac{4\beta - 1}{3} f + \beta \xi \frac{df}{d\xi} = 0, \quad f = \xi^{(4\beta-1)/3\beta} \quad \text{at} \quad \xi = \xi_\infty, \tag{2.15a}$$

$$-\frac{4\beta - 1}{3} f + \beta \xi \frac{df}{d\xi} = 0, \quad f = B \quad \text{at} \quad \xi = \frac{\xi_\infty}{2}, \tag{2.15b}$$

where $B$ is a free parameter. Then, four initial conditions $(f, \; f', \; f'', \; f''')$ can be provided at $\xi = \xi_\infty/2$, and an initial-value problem can be solved toward the origin. Different values of $B$ correspond to different values of $a_1$ in (2.14), thus generating different solutions such as the generic touch-down, non-generic thin-film and blow-up solutions, analogous to the different scenarios identified for $\beta = 2/5$ in figure 3. As a check on our handling of the far field, for $\beta = 2/5$ the non-generic touch-down solution obtained using this method (shown in figure 4a) is indistinguishable from the corresponding solution obtained using the shooting procedure with far-field condition (2.14). In order to resolve the features of the solution near $f = 0$, we used an adaptive ODE solver with a precision of up to thirty digits, implemented in the computer algebra system MAPLE.

We show in figure 4a representative self-similar solutions for $\beta = 0.40, 0.42, 0.44, 0.46, 0.48, 0.50$. By varying $B$, we approach the non-generic solution in which a thin prewetting
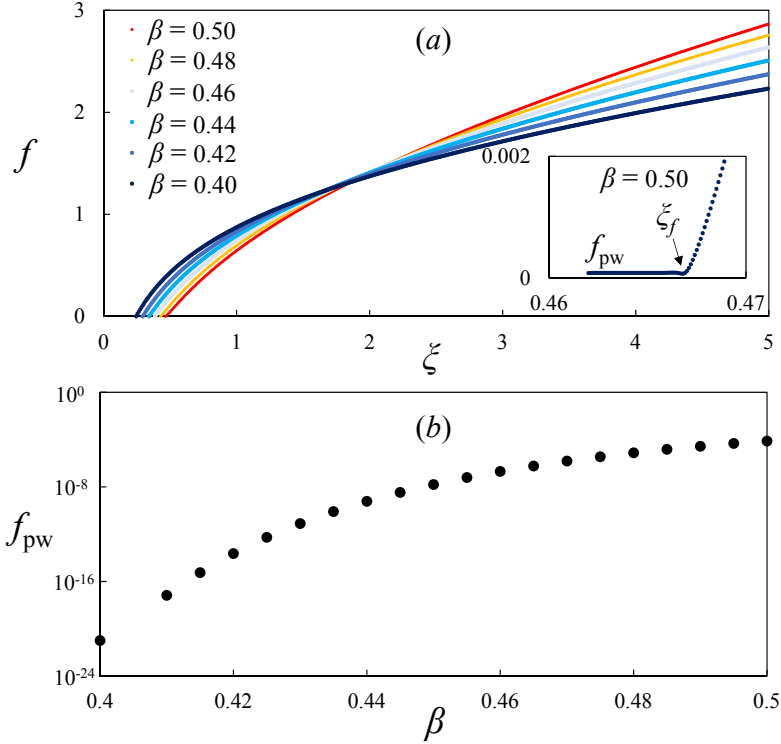
FIGURE 4. Self-similar solutions in the contact-line dominated regime with general values of $\beta$. (*a*) Profile shapes for $\beta = 0.40, 0.42, 0.44, 0.46, 0.48, 0.50$. The slope in the far field increases when $\beta$ increases. Inset: Taking $\beta = 0.50$ as an example, numerical solutions show that a thin prewetting film develops near the contact line. (*b*) The influence of $\beta$ on the thickness of the prewetting film $f_{pw}$ developed toward the origin. The film thickness $f_{pw}$ ranges from $O(10^{-4})$ for $\beta = 0.50$ to $O(10^{-21})$ for $\beta = 0.40$. In all cases, a representative far-field location is chosen as $\xi_\infty = 10$.

film is present, instead of a front ($f = 0$) near the contact line. The film thickness $f_{pw}$ ranges from $O(10^{-4})$ for $\beta = 0.50$ to $O(10^{-21})$ for $\beta = 0.40$, as shown in figure 4*b*. In this case, we can define the apparent front location $\xi_f$ as the location of the local minimum of the profile shapes, by which $\xi_f \approx 0.245$ for $\beta = 0.40$. Here we distinguish between $\xi_f$, the location of the apparent contact line, and $\xi_0$, the actual touchdown point for any given generic solution.

We note that, numerical solutions for ODE (2.10) can also be computed by solving the associated two-point boundary-value problem using numerical continuation, as another alternative procedure. We have carried this out for the case of generic touch-down solutions, with details in Appendix D, and the results agree well with the solutions of the shooting procedure, particularly the relationship between $\beta$ and $f_{pw}$ depicted in figure 4*b*.

### 2.3.3. *Determining $\beta$ from the prewetting film thickness*

The presence of a continuum of self-similar solutions with regard to parameter $\beta$ raises the question how a particular value of $\beta$ is chosen for a given prewetting film thickness $h_{pw}$. Although there is a clear relationship between $\beta$ and the *scaled* prewetting thickness $f_{pw}$, a constant value of $h_{pw}$, arising from the initial condition (2.6), implies a varying

value of $f_{\mathrm{pw}}$, and from the scaling (2.8), the connection is given by

$$h_{\mathrm{pw}} = (t_0 - t)^{(4\beta - 1)/3} f_{\mathrm{pw}}. \tag{2.16}$$

Since $f_{\mathrm{pw}}$ depends on $\beta$, as illustrated in figure 4b, equation (2.16) can be viewed as an equation for $\beta$ as a function of a logarithmic time variable $\tau \equiv -\log(t_0 - t)$. By taking log on both sides of (2.16), we obtain

$$\log h_{\mathrm{pw}} = -\frac{4\beta - 1}{3}\tau + \log f_{\mathrm{pw}}(\beta), \tag{2.17}$$

which yields, upon differentiation with respect to $\tau$,

$$\left(-\frac{4}{3}\tau + \frac{\mathrm{d}}{\mathrm{d}\beta}\log f_{\mathrm{pw}}(\beta)\right)\frac{\mathrm{d}\beta}{\mathrm{d}\tau} = \frac{4\beta - 1}{3}, \tag{2.18}$$

and hence

$$\frac{\mathrm{d}\beta}{\mathrm{d}\tau} = \frac{4\beta - 1}{\left(-4\tau + 3\frac{\mathrm{d}}{\mathrm{d}\beta}\log f_{\mathrm{pw}}(\beta)\right)}. \tag{2.19}$$

We must therefore think of $\beta$ as slowly changing in time, thus our solutions are only "quasi"-self-similar in nature. However, the very fast variation of $f_{\mathrm{pw}}(\beta)$, with $\beta$ depicted in figure 4b, suggests that $\mathrm{d}/\mathrm{d}\beta \log \mathrm{f}_{\mathrm{pw}}(\beta) = O(10^2)$, which results in a small right-hand side in equation (2.19), i.e. $\mathrm{d}\beta/\mathrm{d}\tau = O(10^{-2})$. Thus, the change in $\beta$ will be small when $\tau$ only changes a few units, i.e. when $(t_0 - t)$ only changes for a few decades, which is usually the case in both experiments and numerical simulations.

A more rigorous approach requires an adiabatic approximation, where we write $h(r, t) = (t_0 - t)^{(4\beta(\tau) - 1)/3} f(\tau, \xi)$, and $f(\tau, \xi)$ satisfies the following equation

$$\frac{\partial f}{\partial \tau} + e^{-\tau}\left(\frac{4}{3}f - \xi\frac{\partial f}{\partial \xi}\right)\frac{\mathrm{d}\beta}{\mathrm{d}\tau} - \frac{(4\beta - 1)}{3}f + \beta\xi\frac{\partial f}{\partial \xi} + \frac{1}{\xi}\frac{\partial}{\partial \xi}\left(\xi f^3 \frac{\partial}{\partial \xi}\left(\frac{1}{\xi}\frac{\partial}{\partial \xi}\left(\xi\frac{\partial f}{\partial \xi}\right)\right)\right) = 0. \tag{2.20}$$

After neglecting the terms associated with $\mathrm{d}\beta/\mathrm{d}\tau$ and $\partial f/\partial \tau$, we recover equation (2.10) for the similarity solutions, except that now $\beta(\tau)$ is a slowly varying parameter evolving according to equation (2.19).

Given the exponent $(4\beta - 1)/3 < 1$, the factor $(t_0 - t)^{(4\beta - 1)/3}$ in (2.16) is of order unity, so the order of magnitudes of $f_{\mathrm{pw}}$ and $h_{\mathrm{pw}}$ will match except for when $t$ is very close to $t_0$. From an experimental perspective, we will observe an apparent power law (thus a value for $\beta$), from which we can derive an appropriate order of magnitude for $f_{\mathrm{pw}}$ and hence $h_{\mathrm{pw}}$ through the curve in figure 4b. In other words, once $h_{pw}$ is provided in an experiment or numerical simulation, a corresponding scaling exponent $\beta$ will be observed.

### 2.3.4. *The special value* $\beta = 2/5$

As well as producing the convenient far-field behaviour (2.14), the value $\beta = 2/5$ also has the property of exhibiting a constant, non-zero flow rate far from the front of a healing film. A non-zero flow rate must be sustained away from the hole during the healing process in order to fill the hole with liquid. Setting the flow rate to be constant, or equivalently, $\partial h/\partial t = 0$, in equation (2.5), we obtain the interface shape in the far field

$$h \propto r^{1/2} \text{ for } r \gg r_f(t). \tag{2.21}$$

We note that we have neglected the solutions behaving as $h \propto r^2$ and as $h \propto \ln r$ in the far field, since these solutions correspond to zero flux, whereas the asymptotic behaviour

| experiment | $\mu/\rho$ (cSt) | $\rho$ (kg/m$^3$) | $\gamma$ (mN/m) | $\tilde{h}_0$ (mm) | $\tilde{r}_0$ (mm) | $\tilde{r}_{\mathrm{out}}$ (mm) | $\tilde{t}_0$ (s) |
|:---:|:---:|:---:|:---:|:---:|:---:|:---:|:---:|
| #1 | 500 | 970 | $20.2 \pm 0.8$ | $0.65 \pm 0.05$ | 6.4 | 16.7 | 96 |
| #2 | 500 | 970 | $20.2 \pm 0.8$ | $0.65 \pm 0.05$ | 6.4 | 16.7 | 112 |
| #3 | 20 | 950 | $20.6 \pm 0.8$ | $0.40 \pm 0.05$ | 6.4 | 16.7 | 4.8 |
| #4 | 20 | 950 | $20.6 \pm 0.8$ | $0.15 \pm 0.05$ | 6.4 | 16.7 | 46 |
| #5 | 100 | 960 | $19.9 \pm 0.8$ | $0.65 \pm 0.05$ | 6.4 | 16.7 | 19 |
| #6 | 100 | 960 | $19.9 \pm 0.8$ | $0.65 \pm 0.05$ | 6.4 | 16.7 | 20 |
| #7 | 100 | 960 | $19.9 \pm 0.8$ | $0.36 \pm 0.05$ | 9.5 | 16.7 | 52 |
| #8 | 100 | 960 | $19.9 \pm 0.8$ | $0.53 \pm 0.05$ | 6.4 | 12.7 | 27 |
| #9 | 100 | 960 | $19.9 \pm 0.8$ | $0.80 \pm 0.05$ | 8.0 | 13.0 | 39 |
| #10 | 100 | 960 | $19.9 \pm 0.8$ | $0.80 \pm 0.05$ | 8.0 | 13.0 | 45 |

TABLE 1. Summary of the parameters of the different experiments that we performed of viscous thin films propagating inwardly to fill a hole. We note that we verified that the addition of small amount of dye (Sudan III) does not influence the physical properties such as viscosity, density and surface tension. The viscosity values in this table are provided from the manufacturer. $\tilde{t}_0$ corresponds to the time when the front reaches the origin.

given by (2.21) corresponds to a time-independent flow rate in the far field

$$F \equiv 2\pi r h^3 \frac{\mathrm{d}}{\mathrm{d}r}\left(\frac{1}{r}\frac{\mathrm{d}}{\mathrm{d}r}\left(r\frac{\mathrm{d}h}{\mathrm{d}r}\right)\right). \tag{2.22}$$

Thus, the equivalent far-field behaviour in the self-similar solutions has $f \propto \xi^{1/2}$, which corresponds to the value $\beta = 2/5$. We will see some experimental and computational evidence in § 3 and § 4 that the exponent $\beta = 2/5$ influences the profile shape of the film away from the contact line.

## 3. Experimental observations

In this section, we describe our laboratory experiments of inward spreading liquid films and compare the experimentally obtained time-dependent front locations and profile shapes with the self-similar solutions from the theoretical model (§ 2).

### 3.1. *Experimental setup and calibration*

A schematic of our experimental setup is depicted in figure 5$a$. We first prepare a clean oil-wetting slide glass as a flat substrate, with an LED panel placed below to provide a uniform back lighting. We then place a rubber container above the slide glass to form a circular outer boundary. A rubber cylinder, as a cylindrical lock gate, is then placed at the centre of the circular area surrounded by the outer boundary. A digital camera (Nikon 7100) or an inverted fluorescence microscope (DMI4000B, Leica) is placed above the setup, and photographs are taken from the top. The microscope has a smaller range ($0 \text{ mm} \leqslant \tilde{r} \leqslant 2.5 \text{ mm}$) but a much higher resolution, so is used to measure the profile shape evolution when the hole is small.

In each experiment, we first fill the gap between the lock gate (rubber cylinder) and the outer boundary (rubber container) with a viscous fluid. We use silicone oils with
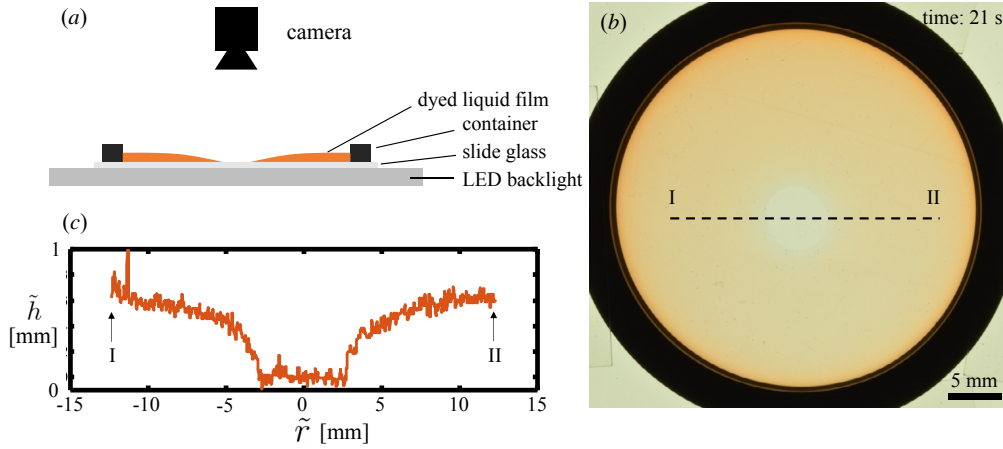
FIGURE 5. Experimental setup to measure the front location and film thickness of healing liquid films. (*a*) A camera or a microscope is placed at the top of the inwardly spreading liquid film. A small amount of dye is added to the liquid film. (*b*) A representative image taken by the digital camera, using silicone oil (500 cSt) as the spreading liquid. The difference in the colour intensity indicates the difference in the film thickness at different locations. (*c*) The profile shape (along the straight line I-II of panel (b)) can be reconstructed based on a calibration that links the intensity with the film thickness.
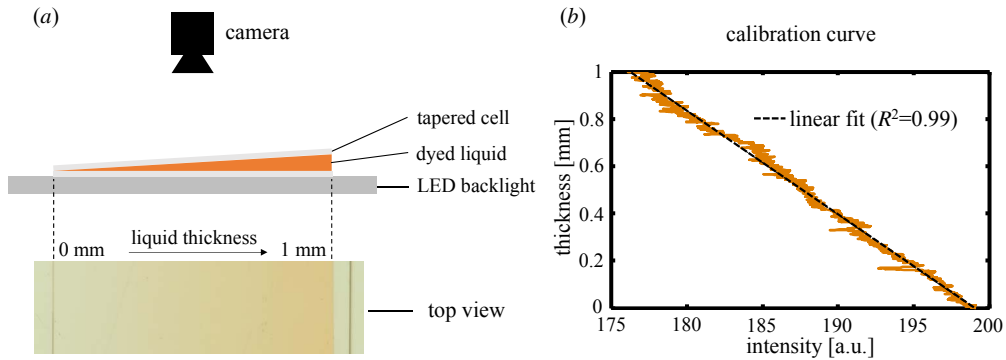


FIGURE 6. Calibration experiments: (*a*) experimental setup; (*b*) calibration curve. A tapered cell filled with dyed liquid was used for the calibration experiments, for example. A representative image (top view) is shown in (*a*), which indicates an intensity change as the thickness of the dyed liquid varies. The relationship between the liquid thickness and image intensity is shown in (*b*), and a linear fit is used for the data analysis.

different viscosities (e.g. Sigma-Aldrich: 20 cSt, 100 cSt, 500 cSt) as the working fluids in our experiments, which do not wet the lock gate and the outer boundary significantly. However, the silicone oils wet the substrate (slide glass), and we expect the existence of a prewetting film. Upon the removal of the lock gate, the liquid spreads inward, filling the hole at the centre. The initial film thickness is chosen to be less than 1 mm. A representative picture (top view) taken by the camera is shown in figure 5*b*. The front of
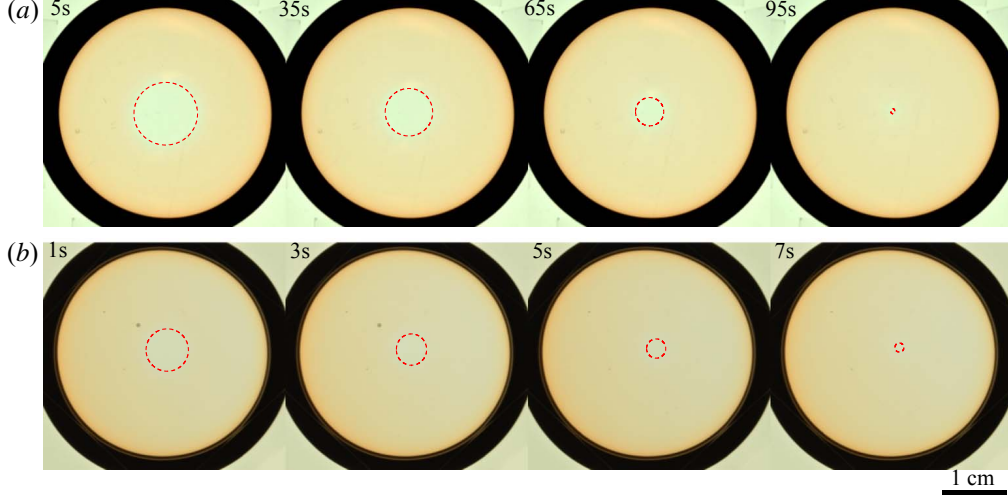
FIGURE 7. Time-dependent images of the inward spreading films in two different experiments: (a) silicone oil 500 cSt (Expt 1 in table 1), and (b) silicone oil 20 cSt (not shown in table 1). The front location is indicated with the dashed line. In both experiments, we kept the same locations for the lock gate ($\tilde{r}_0 \approx 6.4$ mm) and the outer boundary ($\tilde{r}_\text{out} \approx 16.7$ mm). The initial film thickness is (a) $\tilde{h}_0 \approx 0.65$ mm, and (b) $\tilde{h}_0 \approx 0.4$ mm.
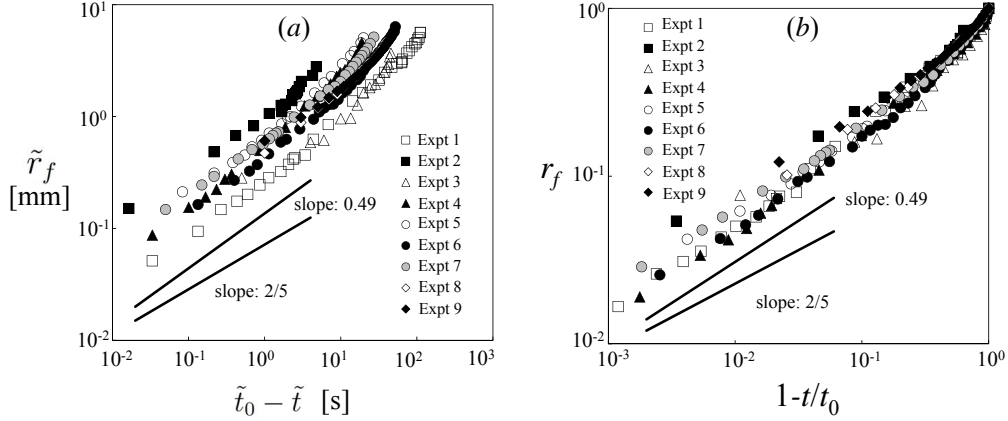


FIGURE 8. Time-dependent front locations from the experimental measurements: (a) raw data and (b) rescaled experimental data. The initial film thickness is chosen to be smaller than or equal to 0.8 mm in this figure. A nonlinear power-law fit of the data in the range $0.01 \leqslant r_f(t) \leqslant 0.2$ provides an exponent of $\beta = 0.489 \pm 0.045$. The slopes of 2/5 and 0.49 in the log-log graph are also shown as the straight lines for reference.

the liquid film is approximately circular, and we can measure the radius of the circular front $\tilde{r}_f(\tilde{t})$ as a function of time, $\tilde{t}$.

A summary of the parameters of the different experiments is given in table 1. To measure the interface shape, we add a small amount of dye (Sigma-Aldrich: Sudan III) to the silicone oils. The dye and silicone oils are well-mixed, and the presence of the dye does not significantly change the viscosity and surface tension. As a result, different film thicknesses correspond to different signal intensities received by the digital camera (see,
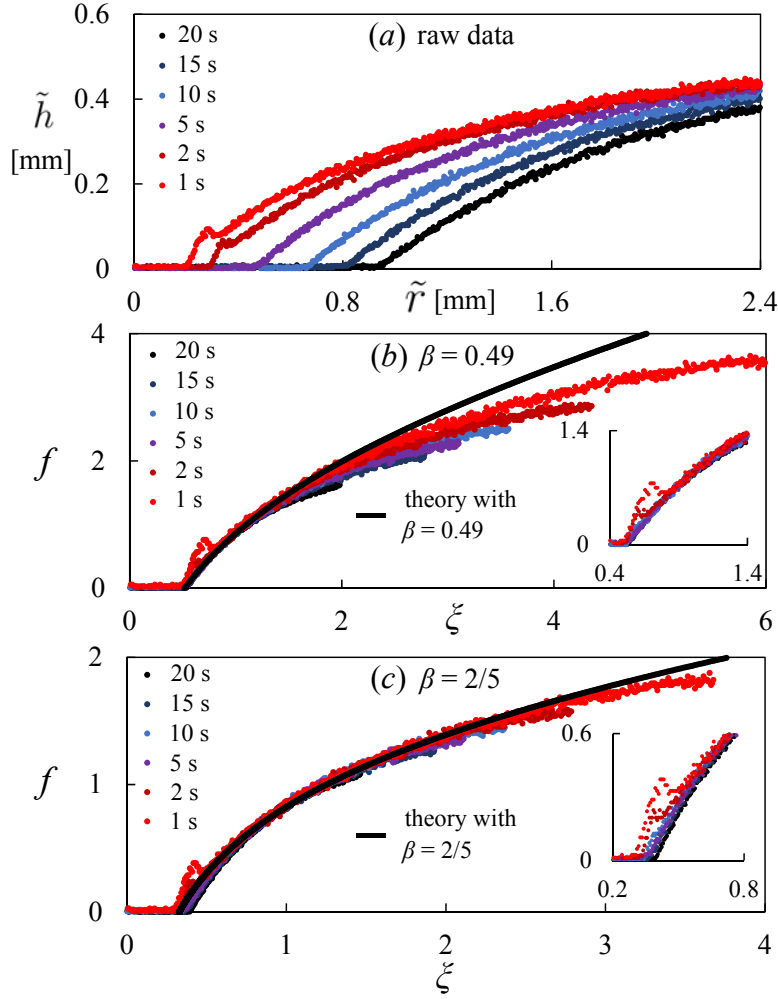
FIGURE 9. Experimental measurement of the time evolution of the profile shape near the touch–down point, using an inverted fluorescence microscope: $(a)$ raw data, $(b)$ rescaled data with $\beta = 0.49$, and $(c)$ rescaled data with $\beta = 2/5$. The theoretical prediction from the self-similar solutions are also shown as the black curves in $(b)$ with $\beta = 0.49$ and $(c)$ with $\beta = 2/5$. The insets in $(b)$ and $(c)$ demonstrate the data collapse of the rescaled profiles near the contact line. The parameters are set to be the same as Expt 1 in table 1. The time listed in the figure indicates the remaining time $\left(\tilde{t}_0 - \tilde{t}\right)$ before the hole eventually closes.

e.g., Bischofberger *et al.* 2014). In addition, we are able to conduct a careful calibration that relates the film thickness to the intensity of the image taken by the digital camera or the microscope, see figure 6 as an example. Then, in our post-experimental data analysis, we reconstruct the profile shapes $\tilde{h}(\tilde{r}, \tilde{t})$ at different times $\tilde{t}$. A representative profile shape is shown in figure 5$c$, which corresponds to the images displayed in figure 5$b$.

### 3.2. *Front location*

As we mentioned above, the time evolution of the location of the propagating front can be obtained from the top view still images, using a digital camera. Typical experimental results showing the closing of the initial hole are shown in figure 7. We note that a drift

can occur in some experiments, as can be seen, for example, in figure 7*b*. However, in all the experiments, the propagating front appears circular as time progresses, which allows us to define the front location $\tilde{r}_f(t)$ based on the radius of the circle, and relocate the origin $\tilde{r} = 0$ at the centre of the circle. In addition, in each experiment, there exists a critical time $\tilde{t}_0$ at which the front reaches the origin, i.e., when $\tilde{r}_f = 0$. Equivalently, $\tilde{t}_0 - \tilde{t}$ represents the time that remains for the front to reach the origin.

The experimental data of $\tilde{r}_f$ versus $\tilde{t}_0 - \tilde{t}$ is shown in figure 8*a*. We also present the non-dimensionalized experimental data of the front location in figure 8*b*. We impose a nonlinear power-law fit for the experimental data in the range $0.01 \leqslant r_f(t) \leqslant 0.2$, which provides an exponent of $0.489 \pm 0.045$. Note that the similarity exponent $\beta \approx 0.49$ corresponds to a value of prewetting thickness $f_{\mathrm{pw}}$ (and hence $h_{\mathrm{pw}}$, as argued in § 2.3.3) of order $10^{-5}$. In addition, $h_{\mathrm{pw}}$ of order $10^{-5}$ corresponds to $\tilde{h}_{\mathrm{pw}}$ of order 10 nm in our experiments, which is consistent with the order of the surface roughness of the substrate (glass slide) and also the typical thickness of prewetting films (see, e.g., Bonn *et al.* 2009). In addition, we note that the observed power law is consistent with the results of the related converging flow experiments and numerical computations of Dijksman *et al.* (2015).

### 3.3. *Profile shape*

Using an inverted fluorescence microscope, we are able to measure the time and space evolution of the profile shapes in our experiments. The time-dependent profile shapes from a representative experiment (Expt 1 in table 1) are shown in figure 9*a*, where silicone oil of viscosity $\mu \approx 500$ cst and surface tension $\gamma \approx 20.2$ mN/m was used.

We then rescale the profile shapes based on the self-similar solution with $\beta = 0.49$, as shown in figure 9*b*, and we observe excellent data collapse in the region close to the contact line. The theoretical prediction with $\beta = 0.49$ is also plotted as the black curve in figure 9*b*, and is found to agree well with collapsed profiles from experimental measurements. The collapse of profile shapes at different times and the agreement with self-similar solutions have not been reported in previous experimental studies on converging films (see, e.g., Dijksman *et al.* 2015).

In addition, we also rescale the raw profiles based on the self-similar solution with $\beta = 2/5$, as shown in figure 9*c*, and the theoretical prediction with $\beta = 2/5$ is also plotted as the black curve. It appears that the $\beta = 2/5$ solution agree well with the rescaled profiles in an intermediate region far away from both the contact line and the outer wall. We note that, as the profiles get close to the outer wall $\tilde{r}_{\mathrm{out}}$, persistent over-prediction of the similarity solutions appears, as the zero-flux boundary condition at $\tilde{r}_{\mathrm{out}}$ becomes more significant. More evidence suggesting the existence of the $\beta = 2/5$ scaling will be provided in § 4.3.2.

### 3.4. *Experimental uncertainty*

There exist various uncertainties in our experimental study, and we briefly mention some of these here. First, while the propagating front appears circular in our experiments, the front may not perfectly lie at the centre of the slide glass (possibly due to the defects of the surface), for example, as shown in figure 7*b*. Secondly, when removing the lock gate, small disturbances can also be introduced, and a small amount of liquid may stick to the lock gate (and leave the system), which modifies the initial condition from being a step function. Further experimental uncertainties occur in the measurement of the viscosity and surface tension of the fluids, the wettability of the lock gate and the outer boundary, and in the calibration that relates the film thickness to the intensity of the pictures.
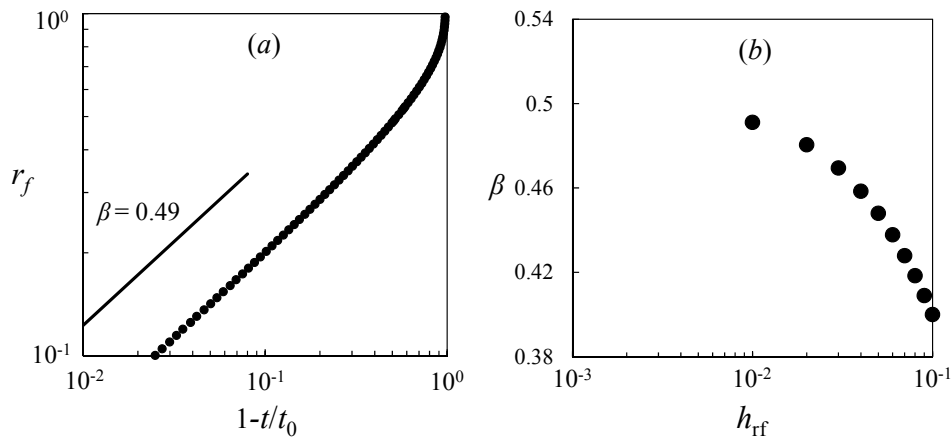
FIGURE 10. The location of the propagating front $r_f(t)$ from a numerical simulation of PDE (2.5) with a prewetting film thickness $h_{pw} = 10^{-5}$, based on the definition of the front location $h(r_f(t), t) \equiv h_{rf}$. (a) The theoretical prediction of $\beta \approx 0.49$ is also plotted as the straight line, which agree well with the numerical data as the hole becomes small (here, $h_{rf} = 0.01$). (b) The scaling exponent $\beta$ as a function of $h_{rf}$: As $h_{rf}$ decreases, the scaling exponent $\beta$ increases toward approximately 0.5. Thus, we set $h_{rf} = 0.01$ as a representative value to define the front location in this study.

We also note that, while the flow is mainly driven by surface tension, buoyancy effects are always present and may play a role in the spreading of the films and the shape of the air-fluid interface. We can estimate the Bond number $Bo \equiv \Delta\rho g \tilde{h}_0^2 / \gamma$, and in a typical experiment, $Bo \approx 980 \times 9.8 \times (0.65 \times 10^{-3})^2 / 0.02 \approx 2$. For this Bond number, the buoyancy effects are found to be negligible from the numerical simulations from a thin-film model, as shown in figure 7 of Dijksman *et al.* (2015).

## 4. Time-dependent computations

In this section, we employ a finite-difference scheme to solve the thin-film equation (2.5), subject to initial and boundary conditions (2.6) and (2.7), respectively, with the outer boundary at $r_{out} = 10$. Details of the numerical scheme are provided in Appendix E. Here, we compare numerical results to the self-similar solutions described in § 2. The numerical scheme was also used to verify another self-similar behaviour at early times, as described in Appendix A.

### 4.1. *Front location*

Since solutions to the PDE (2.5) have a thin prewetting film rather than an actual contact line, we must choose a method to define the location of the propagating front $r_f(t)$ from the numerical solutions. There are two reference heights in the problem: the initial film thickness $h(r_{out}, 0) = 1$, and the prewetting film thickness $h_{pw} \ll 1$. A front $r_f(t)$ can be defined as the value of $r$ that corresponds to a small reference value $h_{rf}$ of the film thickness, i.e. $h(r_f(t), t) = h_{rf}$. Using this method, we show $r_f(t)/r_0$ as a function of $1 - t/t_0$ for $h_{rf} = 0.01$, as an example, in figure 10a, from a numerical simulation in which $h_{pw} = 10^{-5}$. In this case, a slope of $\beta \approx 0.49$ is predicted from the theory, as discussed in § 2.3.3, and the simulationl data agree well with this theoretical prediction as the front propagates toward the origin.

We also vary the value of $h_{rf}$, and show the sensitivity of the estimate of $\beta$ as a
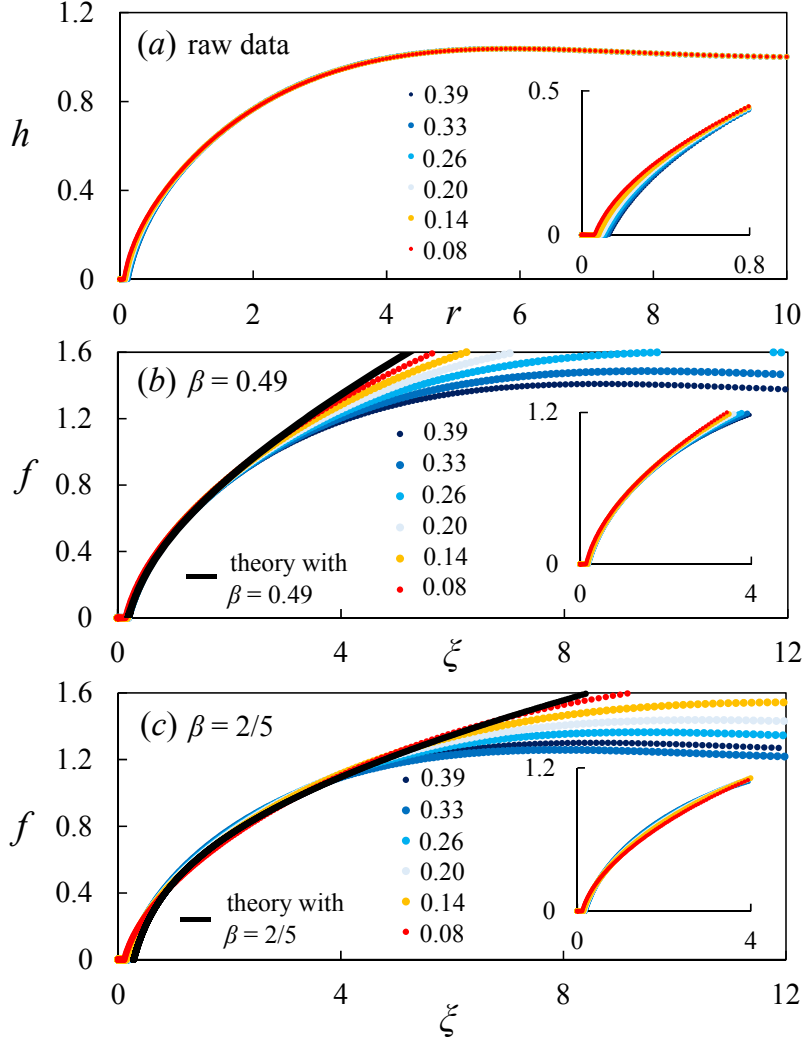
FIGURE 11. Time evolution of the profile shapes near the healing time $t_0 \approx 7.36$ from time-dependent computation of PDE (2.5): (*a*) raw data, (*b*) rescaled data with $\beta = 0.49$, (*c*) rescaled data with $\beta = 2/5$. The numbers in the legends indicate the remaining time $(t_0 - t)$ before the hole eventually closes. Near the contact line, the rescaled profiles agree excellently with the prediction of the self-similar solution with $\beta = 0.49$, shown as the solid curve in (*b*). Away from the contact line region, the $\beta = 2/5$ solution seems to agree with the rescaled profiles, as shown in (*c*). The insets show the profile shapes near the contact line. The thickness of the prewetting film is $h_{\mathrm{pw}} = 10^{-5}$ in the numerical simulation, and the definition of the front is based on $h_{\mathrm{rf}} = 0.01$.

function of $h_{\mathrm{rf}}$ in figure 10*b*. As $h_{\mathrm{rf}}$ decreases, the scaling exponent $\beta$ increases toward a value of approximately 0.5, which is consistent with the time-dependent computations of Dijksman *et al.* (2015), who used a more sophisticated technique to estimate the power-law exponents. Thus, we set $h_{\mathrm{rf}} = 0.01$ as a representative value in the definition of the front location in this study. We also performed time-dependent computations of PDE (2.5) subject to different prewetting film thickness $h_{\mathrm{pw}}$ in the initial condition (2.6), and the dependence of $\beta$ on $h_{\mathrm{pw}}$ will be discussed later in § 4.3.1.
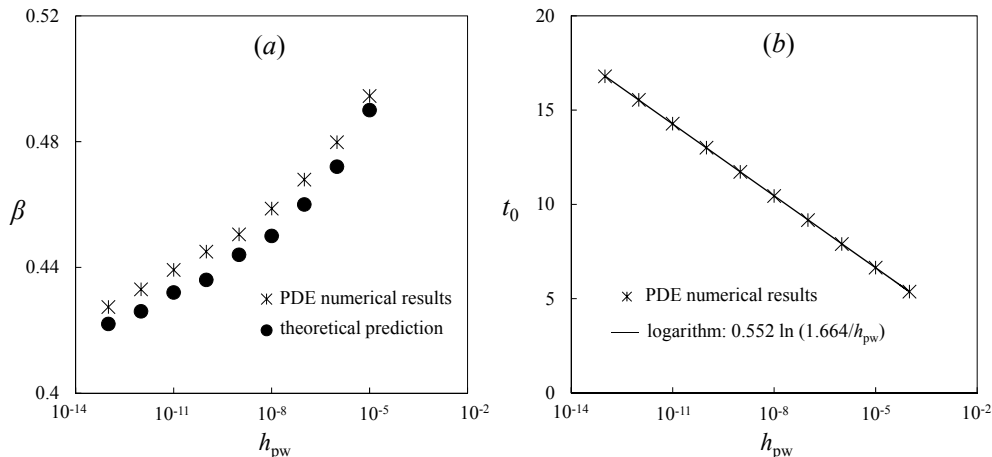
FIGURE 12. Influence of the thickness of the prewetting film $h_{pw}$ on (*a*) the scaling exponent $\beta$ and (*b*) the healing time $t_0$. (*a*) A thinner prewetting film corresponds to a smaller value of scaling exponent $\beta$, which is also consistent with the theoretical calculations as described in § 2.3.3. (*b*) A thinner prewetting film corresponds to a greater healing time $t_0$, and the numerical data suggests a logarithmic fit for the dependence of $t_0$ on $h_{pw}$.

### 4.2. *Profile shape*

Profile shapes at times close to healing are shown in figure 11*a* from the same time-dependent computation depicted in figure 10*a*. The touch-down time is found to be $t_0 \approx 7.36$. In figure 11*b*, we rescale the profile shapes based on the prediction of the self-similar solution with $\beta = 0.49$, and we observe good data collapse near the contact line. In addition, we plot the self-similar solution with $\beta = 0.49$ as the solid curve, which exhibits excellent agreement with the collapsed profile shapes.

The raw profiles in figure 11*a* are also rescaled based on the self-similar solution with $\beta = 2/5$, as shown in figure 11*c*. Similar to the experimental measurments, as shown in figure 9*c*, we observe data collapse in an intermediate region away from both the contact line and the outer wall. The $\beta = 2/5$ similarity solution is also plotted in the same figure, and we observe good agreement in the intermediate region. We provide more discussions on the evidence of the $\beta = 2/5$ scaling in § 4.3.2.

### 4.3. *Discussions*

#### 4.3.1. *Influence of prewetting film thickness $h_{pw}$*

Multiple time-dependent computations have been performed for the PDE (2.5), subject to initial conditions (2.6) with different values of the prewetting film thickness $h_{pw}$, so as to examine the dependence of the scaling exponent $\beta$ and the healing time $t_0$ on the value of $h_{pw}$. The result for the scaling exponent $\beta$ is shown in figure 12*b*, which indicates that $\beta$ increases monotonically with $h_{pw}$. Here, the value of $\beta$ is identified using a nonlinear power-law fit for the numerical data of the front location $r_f(t)$ versus $(t_0 - t)$, and we choose $r_f(t)$ in the range $0.01 \leqslant r_f(t) \leqslant 0.2$. We note that the case of $h_{pw} = 10^{-4}$ is also studied in Dijksman *et al.* (2015), and the authors found $\beta \approx 0.5$ in their time-dependent computations of a thin-film PDE, which is in agreement with our calculations.

We also provide the theoretical calculation of the scaling exponent $\beta$ for different $h_{pw}$, and plot the results in figure 12*b*. The theoretical predictions for $\beta$ are found to be in good qualitative agreement with the results from time-dependent computations, while
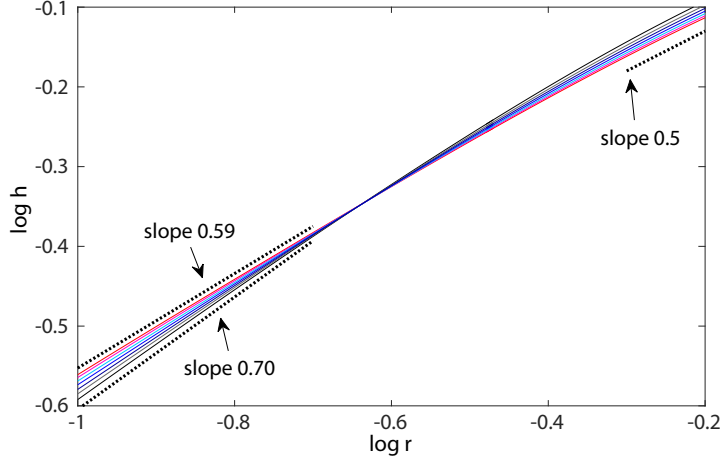
FIGURE 13. Interface profiles in a logarithmic scale when $r_f = 10^{-3}$ with different thicknesses for the prewetting film $h_{\mathrm{pw}} = 10^{-10}$, $10^{-9}$, $10^{-8}$, $10^{-7}$, $10^{-6}$, $10^{-5}$ and $10^{-4}$. Note the presence of power laws with scaling exponents $(4\beta - 1)/3\beta$ from 0.59 $\left(\text{for } h_{\mathrm{pw}} = 10^{-10}\right)$ to 0.70 $\left(\text{for } h_{\mathrm{pw}} = 10^{-4}\right)$ near the contact line region, and a transition to a $1/2$ power law (i.e., $\beta = 2/5$) that is independent of $h_{\mathrm{pw}}$ away from the contact-line region.
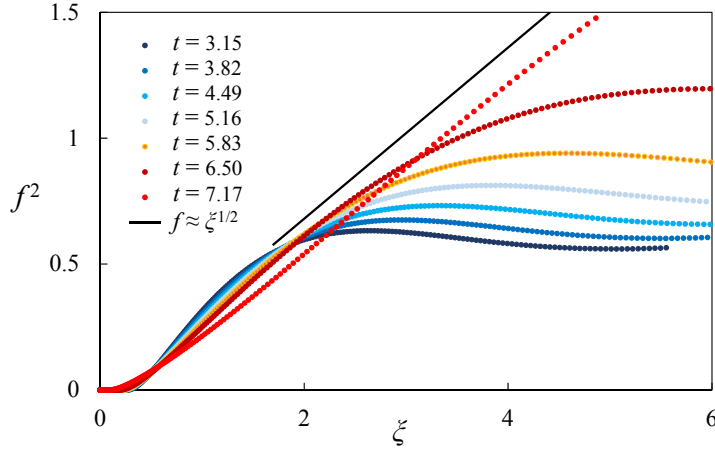


FIGURE 14. Rescaled interface profiles $\left(r, h^2\right)$ from $r_f \approx 0.46$ down to $r_f \approx 0.04$ with time intervals $\Delta t \approx 0.67$. The rescaling is based on $\beta = 2/5$, i.e. $\xi = r/(t_0 - t)^{2/5}$, and $f^2 = h^2/(t_0 - t)^{2/5}$. Notice that the convergence of the rescaled profile shapes to a straight line away from the contact line when $t \to t_0$. Near the contact line, the profiles do not converge as expected, since the scaling with a different exponent $\beta$ holds there.

the theoretical calculations are slightly smaller than the results from data fitting of the time-dependent computations. Note that, in the theoretical calculation, to estimate $f_{\mathrm{pw}}$ from a given $h_{\mathrm{pw}}$, we use (2.16) using a representative time $t_r = 0.99t_0$ close to healing (the estimate is only weakly dependent on this choice).

In addition, we show the dependence of the healing time $t_0$ on $h_{\mathrm{pw}}$ in figure 12a. From the time-dependent computations, we found that $t_0$ increases logarithmically with $h_{\mathrm{pw}}$. Such a dependence is common in contact-line problems, where the velocity of a moving
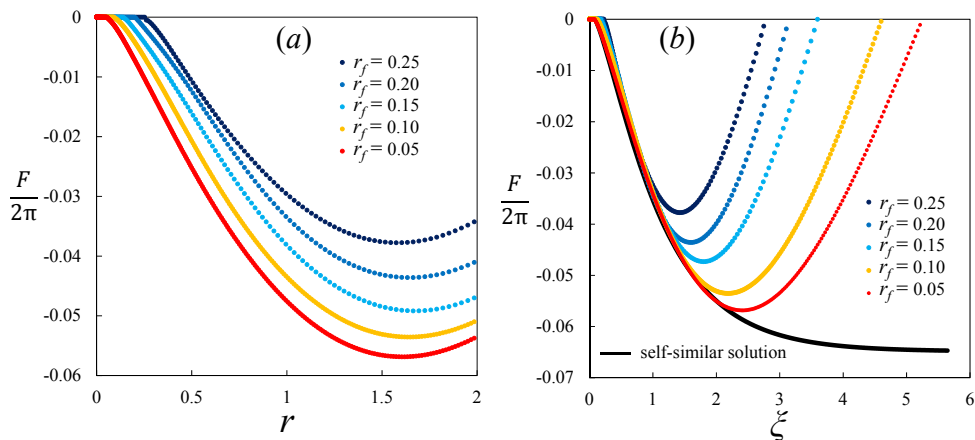
FIGURE 15. Time evolution of the flow rate $F$ from direct numerical simulation: ($a$) raw data, and ($b$) rescaled data. The collapse of the flow rate data occurs in the region near the propagating front, but not too close to the contact line. Here the thickness of the prewetting film is $h_{\mathrm{pw}} = 10^{-5}$, and the definition of the front is based on $h_{\mathrm{rf}} = 0.01$. The curve represents the prediction from a self-similar solution with $\beta = 2/5$.

contact line is logarithmically dependent on a small regularizing parameter, which, in our case, is the prewetting film thickness $h_{\mathrm{pw}}$.

### 4.3.2. *Evidence of the $\beta = 2/5$ scaling*

The profile shape measurements in both laboratory experiments (figure $9c$) and time-dependent computations (figure $11c$) suggest the existence of a self-similar solution with $\beta = 2/5$ in an intermediate region away from both the contact line and the outer wall. Here we provide more evidence of the $\beta = 2/5$ scaling from the time-dependent computations.

We first show in figure 13 the interface profile versus the distance to the centre (both in logarithmic scale) for various values of $h_{\mathrm{pw}}$ and at a particular time when the front is at a distance $r_f = 10^{-3}$ from the centre. It is evident that very well-defined power laws, depending on the value of $\beta$, appear in the vicinity of the contact line. The thickness of the prewetting layer considered here ranges from $10^{-10}$ to $10^{-4}$, and the observed exponents for $h(r,t)$ range from 0.59 to 0.70, which correspond to the value of $\beta$ from 0.45 to 0.53. This is consistent with the dependence of $\beta$ on $h_{\mathrm{pw}}$, as shown in figure $12a$.

On the other hand, sufficiently far from the contact line but before the boundary effects at $r_{\mathrm{out}}$ become important, the interface shape behaves as $h \propto r^{1/2}$, as shown in figure 13, and such behaviour is independent of the thickness of the prewetting layer $h_{\mathrm{pw}}$. To further verify this power law, we rescale the profile shapes at different times according to $\left(\xi, f^2\right) = \left(r/(t_0 - t)^{2/5}, h^2/(t_0 - t)^{2/5}\right)$, as shown in figure 14. The profiles $\left(\xi, f^2\right)$ approach a straight line as $t \to t_0$, which indicates the approach of $h$ toward the asymptotic behaviour of $h \propto r^{1/2}$. We also observe the absence of convergence of the interface profiles near the contact line in figure 14, which is consistent with the argument that the 2/5 scaling fails near the contact line.

In addition, from the time-dependent computations of the PDE (2.5), the evolution of the flow rate is available, as defined by equation (2.22), which can also be used to investigate the $\beta = 2/5$ scaling. The flow rate remains maximum (in absolute value) at an approximately constant distance from the origin, as shown in figure $15a$, and its value decreases but is bounded from below as $r_f \to 0^+$. We further compare the results of the

flow rate with the prediction of a $\beta = 2/5$ self-similar solution by rescaling the horizontal axis by $(t_0 - t)^{2/5}$ in figure 15$b$. We observe good data collapse in an intermediate region away from both the contact line and the outer boundary, and also good agreement with the prediction of a self-similar solution with $\beta = 2/5$.


## 5. Summary and discussions

We presented a combined analytical, numerical and experimental study of the healing process of a thin viscous film driven by surface tension, i.e. the inward spreading process of a liquid film in a container to fill a hole in the centre. Such a situation exists in a wide spectrum of natural and industrial applications such as the self-healing, spin coating, surfactant spreading, and glass transition processes.

The analytical study was based on a well-known fourth-order differential equation of the evolution type for the film thickness that is valid in the thin-film/lubrication approximation. In addition, to resolve the stress singularity at the moving contact line, we introduced a thin prewetting liquid film in the problem, via the initial condition, which is assumed to move hydrodynamically with the bulk liquid behind the contact line (see, e.g., Tanner 1979; Kataoka & Troian 1997; Levy & Shearer 2004; Savva & Kalliadasis 2011; Eggers & Fontelos 2015). Such a thin prewetting film might be generated, for example, by van der Waals forces or diffusion (see, e.g., Snoeijer & Andreotti 2013). We did not attempt to justify the microscopic origin of this layer here, but merely used it to regularize the stress singularity. We do note however, that using elements from the statistical mechanics of classical fluids it can be shown that a "liquid-like" film (i.e. a film with density between the liquid and its vapor), due to adsorption of liquid molecules on the substrate, is always present due to the attractive part in the liquid-solid interaction (if the interaction were fully repulsive there would be no contact with the substrate) (e.g. Yatshyshin *et al.* 2016). Statistical mechanics can also be used to obtain the precise form of the associated disjoining pressure (Yatsyshin *et al.* 2015). The influence of the various forms of van der Waals interactions on the precursor layer and their overall effects on the healing process will be the subject of future work.

For the hole healing process, the velocity increases and becomes unbounded as the hole closes, so there is no longer a clear separation of time scales. Thus, instead of assuming quasi-steadiness for the hole healing dynamics (see, e.g., Bostwick *et al.* 2017), we employed a self-similar ansatz to predict the power-law decay of the hole radius, as well as the film profile. As far as later stages of the healing are concerned, we found that the profile shapes are described by solutions of an ODE that contains one similarity exponent, $\beta$. We computed solutions to the similarity equation with different values of $\beta$, and found that the solutions can exhibit five distinct near-field behaviours: blow-up, generic touch-down, touch-down at the origin, a thick film, and a non-generic critical behaviour that separates the generic touch-down solutions from the generic blow-up ones. These observations were supported by the asymptotic analysis of the solutions in the near field. We suggested that the non-generic critical solution is the one that describes the healing process. In addition, the similarity exponent $\beta$ is not determined purely from scaling arguments. Instead, $\beta$ becomes a function of the finite thickness of the prewetting film, which we determine numerically. Thus, the solutions we obtained are self-similar solutions of the second kind.

We also performed time-dependent computations for the full PDE that describes the evolution of the interface. There is very good agreement for both the front location and the profile shapes near the contact line between the numerical results and the self-similar solutions that predict the correct thickness of the prewetting film. A systematic study

of the dependence of the exponent $\beta$ on the thickness of the prewetting film was also performed and very good agreement was obtained between the theoretical prediction and the results of time-dependent computations. Further, we designed and conducted laboratory experiments of healing liquid films in the regime where surface tension dominates the spreading. A comparison between the experimental observations and theoretical predictions for the profile shape and front location further supports the existence of the late-time self-similar solutions we obtained. The theoretical framework can also be extended to study the hole healing processes in other practical contexts such as the spreading of floating liquid layers (see, e.g., Lister & Kerr 1989; Feng *et al.* 2014) and surfactants (see, e.g., Jensen 1994).

## Acknowledgment

## Appendix A. Early-time dynamics

While our focus in this study is on the behaviour of the film close to the time when it heals, it is also interesting to analyse the early-time relaxation from the initial step condition (2.6). The initial behaviour occurs in a small region near the step at $r = 1$, and it is appropriate to use the approximation $r = \rho + 1$, with $\rho \ll 1$, so that the early-time dynamics of spreading is described by

$$\frac{\partial h}{\partial t} + \frac{\partial}{\partial \rho}\left(h^3 \frac{\partial^3 h}{\partial \rho^3}\right) = 0. \tag{A 1}$$

Thus, the early dynamics near $t = 0$ can be approximated by a self-similar solution in the form $h(\rho, t) = H(\eta)$, where $\eta = \rho/t^{1/4}$. The scaled profile $H$ satisfies

$$-\frac{1}{4}\eta \frac{\mathrm{d}H}{\mathrm{d}\eta} + \frac{\mathrm{d}}{\mathrm{d}\eta}\left(H^3 \frac{\mathrm{d}^3 H}{\mathrm{d}\eta^3}\right) = 0, \tag{A 2}$$

while appropriate boundary conditions are, from (2.6),

$$H = h_{\mathrm{pw}}, \ \frac{\mathrm{d}H}{\mathrm{d}\eta} = 0 \text{ as } \eta \to -\infty, \tag{A 3a}$$

$$H = 1, \ \frac{\mathrm{d}H}{\mathrm{d}\eta} = 0 \text{ as } \eta \to +\infty. \tag{A 3b}$$

For a given $h_{\mathrm{pw}}$, (A 2) with (A 3) may be solved numerically as a boundary-value problem on a sufficiently large domain. An example solution is plotted in figure 16 for $h_{\mathrm{pw}} = 0.02$. For verification, we compare this solution to a numerical solution of the full problem (2.5)–(2.7) and obtain very good agreement. A description of the numerical method to solve the full problem is given in Appendix E. For the numerical solution of (2.5), we set $r_{\mathrm{out}} = 10$, while in computing the self-similar solution from equation (A 2), we set $\eta = \pm 10$ as the far-field locations.
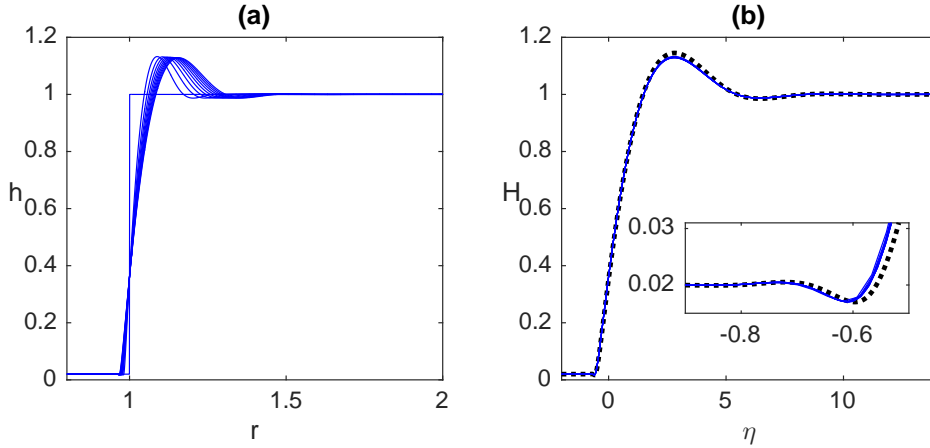
FIGURE 16. Time evolution of the profile shape $h(r,t)$ at early times, $0 < t < 10^{-5}$: (*a*) unscaled profiles, and (*b*) scaled profiles, compared to the self-similar profile (dotted curve). The self-similar solution agrees well with the numerical solutions at early times.

The main feature of the solutions depicted in figure 16 is the creation of capillary oscillations on both sides of the initial step. On the side of the thick film ($r > 1$) a large capillary ridge forms, which moves towards the outer boundary, while on the side of the prewetting film ($r < 1$) the small oscillations preceding the moving (apparent) contact line are reminiscent of those that exist in related problems (see, e.g., Bertozzi *et al.* 1994; Eggers & Fontelos 2015), such as the linear problem that describes the dynamics of flexible filaments in a viscous fluid (Stone & Duprat 2016), and the Bretherton problem (Bretherton 1961), in which a thin prewetting film connects to an advancing apparent contact line. We also note that, although the thin-film model equation is strictly speaking valid for small interfacial slopes and is expected to break down when interfacial slopes are large, experimental work appears to support the use of thin-film models to describe the relaxation process from step initial shapes (see, e.g., Huppert & Woods 1995; McGraw *et al.* 2012).

## Appendix B. Far-field asymptotics

Here we analyse the asymptotic behaviour of the solutions of (2.10) for the special value $\beta = 2/5$ in the far field (i.e. as $\xi \to \infty$). First, we note that $f = \xi^{1/2}$ is an exact solution, as mentioned in § 2.2. Thus, we impose the far-field behaviour in the form

$$f(\xi) = a_1 \xi^{1/2} + \tilde{f}(\xi) \quad \text{as} \quad \xi \to \infty, \tag{B 1}$$

where $|\tilde{f}(\xi)| \ll \xi^{1/2}$.

For simplicity and without loss of generality, we impose $a_1 = 1$. Then, we substitute (B 1) in (2.10) and obtain the following linearized equation:

$$-\frac{1}{5}\tilde{f} + \frac{2}{5}\xi\frac{d\tilde{f}}{d\xi} + \frac{1}{\xi}\frac{d}{d\xi}\left(-\frac{9}{8}\xi^{-1/2}\tilde{f} + \xi^{5/2}\frac{d}{d\xi}\left[\frac{1}{\xi}\frac{d}{d\xi}\left(\xi\frac{d\tilde{f}}{d\xi}\right)\right]\right) = 0, \tag{B 2}$$

which can be simplified to the form

$$\xi^{3/2}\frac{d^4\tilde{f}}{d\xi^4} + \frac{7}{2}\xi^{1/2}\frac{d^3\tilde{f}}{d\xi^3} + \frac{1}{2}\xi^{-1/2}\frac{d^2\tilde{f}}{d\xi^2} + \frac{2}{5}\xi\frac{d\tilde{f}}{d\xi} - \frac{1}{5}\tilde{f} = 0. \tag{B 3}$$

Next, we employ a WKB strategy, and make the following substitution

$$\tilde{f} = e^{-W}. \tag{B 4}$$

Assuming that $W'' \ll (W')^2$, $W''' \ll (W')^3$, and $W'''' \ll (W')^4$, where $'$ denotes $\mathrm{d}/\mathrm{d}\xi$, (B 3) can be simplified to the equation

$$\xi^{3/2}(W')^4 - \frac{7}{2}\xi^{1/2}(W')^3 + \frac{1}{2}\xi^{-1/2}(W')^2 - \frac{2}{5}\xi W' - \frac{1}{5} = 0. \tag{B 5}$$

We further make the substitution

$$W' = \xi^{-1/6}V. \tag{B 6}$$

Then, (B 5) can be rewritten as

$$\xi^{5/6}V^4 - \frac{7}{2}V^3 + \frac{1}{2}\xi^{-5/6}V^2 - \frac{2}{5}\xi^{5/6}V - \frac{1}{5} = 0, \tag{B 7}$$

and the leading-order balance is

$$\xi^{5/6}V^4 - \frac{2}{5}\xi^{5/6}V = 0, \tag{B 8}$$

which provides three non-trivial solutions for $V$:

$$V = \left(\frac{2}{5}\right)^{1/3}, \quad \left(\frac{2}{5}\right)^{1/3} e^{\pm 2\pi i/3}. \tag{B 9}$$

The two complex roots are neglected since they lead to $\tilde{f}(\xi)$ being highly oscillatory and growing faster than any power-law behaviour. To compute the next-order contribution to $V$, we write

$$V = \left(\frac{2}{5}\right)^{1/3} + \tilde{V}(\xi), \tag{B 10}$$

where $|\tilde{V}| \ll 1$, and, substituting (B 10) in (B 7), can obtain

$$\tilde{V} = \frac{8}{5}\xi^{-5/6}. \tag{B 11}$$

Substituting (B 10) and (B 11) in (B 6), we can obtain the asymptotic expression in the far field for $W(\xi)$:

$$W = \frac{6}{5}\left(\frac{2}{5}\right)^{1/3}\xi^{5/6} + \frac{8}{5}\ln\xi + O(1), \tag{B 12}$$

and also the asymptotic expression for $\tilde{f}(\xi)$ using (B 4) and for $f(\xi)$ using (B 1) with $a_1 = 1$:

$$f(\xi) \sim \xi^{1/2} + \tilde{a}_2\xi^{-8/5}e^{-(6/5)(2/5)^{1/3}\xi^{5/6}} \quad \text{as} \quad \xi \to \infty, \tag{B 13}$$

where $\tilde{a}_2$ is a constant.

We remind that to obtain (B 13) we set $a_1 = 1$ in (B 1) for simplicity (but without loss of generality). In fact, due to the invariance of (2.10) for $\beta = 2/5$ under the transformation $f \mapsto \lambda f$, $\xi \mapsto \lambda^{3/4}\xi$, where $\lambda$ is a positive constant, we obtain the following more general asymptotic behaviour of $f(\xi)$ as $\xi \to \infty$:

$$\lambda f(\xi) \sim \left(\lambda^{3/4}\xi\right)^{1/2} + \tilde{a}_2\left(\lambda^{3/4}\xi\right)^{-8/5}e^{-(6/5)(2/5)^{1/3}\left(\lambda^{3/4}\xi\right)^{5/6}}, \tag{B 14}$$

which can be rearranged to the form

$$f(\xi) \sim a_1\xi^{1/2} + a_2\xi^{-8/5}e^{-(6/5)(2/5)^{1/3}a_1^{-1}\xi^{5/6}} \quad \text{as} \quad \xi \to \infty, \tag{B 15}$$

where $a_1 \equiv \lambda^{-5/8}$ and $a_2 \equiv \tilde{a}_2 \lambda^{-11/5}$.

## Appendix C. Near-field asymptotics

### C.1. *Asymptotics for touch-down at the origin*

If $f \to 0$ as $\xi$ approaches the origin, then in general,

$$f \sim \frac{3}{20}(75\alpha - 100\beta)\xi^{4/3}, \tag{C1}$$

while if $\beta = 2/5$ there is also the special behaviour $f \sim c\xi^{1/2}$ for any $c$, as this is an exact solution over all $\xi$.

### C.2. *Asymptotics for the blow-up solutions*

Next, we analyse the asymptotic behaviour of solutions of (2.10) that blow up at the origin. We first assume the power-law form $f \sim b_1 \xi^\gamma$ with $\gamma < 0$. Substituting this expression in (2.10), we obtain the leading-order behaviour of each term:

$$-\frac{4\beta-1}{3}f+\beta\xi f' \sim \left(-\frac{4\beta-1}{3}+\beta\gamma\right)b_1\xi^\gamma, \qquad \frac{1}{\xi}\left[\xi f^3\left(\frac{1}{\xi}(\xi f')'\right)'\right]' \sim \gamma^2(\gamma-2)b_1\xi^{4\gamma-2}. \tag{C2}$$

No balance is possible for negative $\gamma$, so $f$ does not behave as a simple power law.

We therefore assume a general power-law-logarithmic expansion of the form

$$f \sim \sum_{j=1}^{\infty} b_j \xi^{\gamma_j}(-\log\xi)^{\Delta_j}, \tag{C3}$$

where $\gamma_1 \leqslant 0, \Delta_1 > 0$ is required for blow-up. Substitution of (C3) into the terms in (2.10) gives the leading order behaviour

$$-\frac{1}{5}f + \frac{2}{5}\xi f' \sim \left(-\frac{4\beta-1}{3}+\beta\gamma_1\right)b_1\xi^{\gamma_1}(-\log\xi)^{\Delta_1}, \tag{C4}$$

$$\frac{1}{\xi}\left[\xi f^3\left(\frac{1}{\xi}(\xi f')'\right)'\right]' \sim \gamma_1^2(\gamma_1-2)(4\gamma_1-2)b_1^4\xi^{4\gamma_1-4}(-\log\xi)^{4\Delta_1}, \qquad \gamma_1 \neq 0. \tag{C5}$$

The second term (C5), resulting from the surface tension term in (2.10), is too singular to match with (C4) with $\gamma_1 \neq 0$, so we must have $\gamma_1 = 0$. Taking $\gamma_1 = 0$, the asymptotic behaviour is

$$\frac{1}{\xi}\left[\xi f^3\left(\frac{1}{\xi}(\xi f')'\right)'\right]' \sim 4b_1^4\Delta_1(\Delta_1-1)\frac{(-\log\xi)^{4\Delta_1-2}}{\xi^4}, \qquad \Delta_1 \neq 0,1. \tag{C6}$$

Again, this is too singular to match with (C4), so $\Delta_1 = 1$. The coefficient $b_1$ is arbitrary.

Continuing this process, we find that the exponents of the first three terms are determined in a similar manner: $(\gamma_2, \Delta_2) = (0,0)$, $(\gamma_3, \Delta_3) = (2,0)$, $(\gamma_4, \Delta_4) = (2,-2)$, with $b_2, b_3, b_4$ arbitrary. The fifth term in (C3) does not feature an arbitrary constant, as it must cancel out the $O(\xi^{-2}(-\log\xi)^{-2})$ term introduced by the fourth term in (C3), giving $b_5 = -2b_4(b_1+b_2)/b_1$. The same holds for higher terms, with the first term matching with (C4) occurring at $O(\xi^4(-\log\xi)^{-2})$. We thus obtain the following asymptotic expansion:

$$f \sim b_1(-\log\xi) + b_2 + b_3\xi^2 + b_4\frac{\xi^2}{(-\log\xi)^2} + O\left(\frac{\xi^2}{(-\log\xi)^3}\right), \tag{C7}$$

where $b_1, b_2, b_3, b_4$ are parameters. Note that as a special case it includes thick-film solutions when $b_1 = b_4 = 0$, in which case $f$ is analytic and the error term is $O(\xi^4)$.

### C.3. *Asymptotics near a touch-down point*

In this section, we analyse the asymptotic behaviour of solutions of (2.10) near a touch-down point $\xi_0 > 0$. The leading-order terms of (2.10) near $\xi_0$ are

$$\beta \xi_0 \frac{\mathrm{d}f}{\mathrm{d}\xi} + \frac{\mathrm{d}}{\mathrm{d}\xi}\left(f^3 \frac{\mathrm{d}^3 f}{\mathrm{d}\xi^3}\right) = 0. \tag{C8}$$

Integrating (C8) once provides

$$\beta \xi_0 f + f^3 \frac{\mathrm{d}^3 f}{\mathrm{d}\xi^3} = \epsilon. \tag{C9}$$

We assume the power-law form $f \sim c_1 (\xi - \xi_0)^{\Delta_1} + c_2 (\xi - \xi_0)^{\Delta_2} + \ldots$ with $0 < \Delta_1 < \Delta_2, \ldots$, and $c_1 > 0$. Then, on substitution into (C9) we obtain $\Delta = 3/4$, $c_1 = (64\epsilon/15)^{1/4}$ (or, equivalently, $\epsilon = 15 c_1^4/64$), $\Delta_2 = 3/2$, and $c_2 = -(64\beta\xi_0)/(21 c_1^2)$, thus:

$$f \sim (64\epsilon/15)^{1/4} (\xi - \xi_0)^{3/4} - \frac{8\sqrt{15}\beta\xi_0}{21\sqrt{\epsilon}} (\xi - \xi_0)^{3/2}. \tag{C10}$$

Note that such generic touch-down behaviour occurs only for $\epsilon > 0$. When $\epsilon < 0$, there is no real solution for $c_1$, and we do not have a power-law behaviour touching the $\xi$-axis from above as $\xi \to \xi_0^+$.

Generic touch-down corresponds to $\epsilon > 0$. Note that in the limit $\epsilon \to 0^+$ (or, equivalently, $c_1 \to 0$) the generic touch-down (C10) becomes singular, as the coefficient of the second term blows up. In fact, Duffy & Wilson (1996) have shown that for solutions of (C9) with $\epsilon = 0$, there are no solutions touching down the $\xi$-axis from above as $\xi \to \xi_0^+$. In this case, the behaviour of $f$ near $\xi = \xi_0$ is (assuming $\xi > \xi_0$)

$$f \sim -(3\beta\xi_0)^{1/3} (\xi - \xi_0)[-\log(\xi - \xi_0)]^{1/3}. \tag{C11}$$

This cannot approach the touchdown point from above, so, as with the case where $\epsilon < 0$, this touchdown behaviour does not pertain to the similarity solutions we consider.

Finally, as well as the touch-down solutions, (C9) admits solutions that remain strictly positive. These solutions are also relevant to travelling wave or 'quasi-steady' analysis of moving contact line between a fluid body and a much thinner prewetting film, originally derived by Landau & Levich (1942) (see, also, Myers 1998). The $\xi \gg \xi_0$ behaviour of such solutions is either quadratic $[f \propto (\xi - \xi_0)^2]$ or almost-linear $[f \propto (\xi - \xi_0)\log^{1/3}(\xi - \xi_0)]$ (Bender & Orszag 1978; Eggers 2004). Our numerical results have indicated that the solution to (2.10) with this behaviour matches to the latter behaviour and is unique for a given $\beta$. This solution is approached as $c_1$, say, is reduced to near-zero, as long as $\beta$ is greater than 2/5. The full similarity solution (2.10) does not support the existence of a prewetting film [as constant $f = f_{\mathrm{pw}}$ is not a solution to (2.10)], so the similarity solution can only be assumed to hold in some region near the contact line.

## Appendix D. Self-similar solutions using numerical continuation

The self-similar solutions to the ODE (2.10) were computed using shooting in § 2. Another method of computation is to solve the governing equation as a boundary-value problem on a suitably large domain. Here we compute the solutions to generic touch-down using such a method, implemented in the numerical continuation package AUTO-07p

(Doedel *et al.* 2007). Numerical continuation is a particularly useful and powerful method to use, as it allows us to systematically and efficiently compute the one-parameter family of solutions (parametrized, say, by $\xi_0$) for each exponent $\beta$. We note that numerical-continuation techniques have also been used for computation of self-similar solutions in a related problem of a thin-film rupture on a solid substrate, see Tseluiko *et al.* (2013), Dallaston *et al.* (2017).

Firstly, we compute solutions with a generic touch-down behaviour at $\xi_0$. Since we expect $f \sim c_1(\xi - \xi_0)^{3/4}$, we perform the change of variables

$$\xi = \xi_0 + z^4, \qquad f = z^3 g(z), \tag{D 1}$$

which removes the singularity at $\xi = \xi_0$, so that $g$ is smooth in $z$. Now, we define state variables

$$U_1 = g, \quad U_2 = \frac{\xi_0 + z^4}{4}(zg' + 3g), \quad U_3 = \frac{zU_2' - U_2}{4(\xi_0 + z^4)}, \quad U_4 = \frac{(\xi_0 + z^4)g^3}{4}(zU_3' - 5U_3), \tag{D 2}$$

(where $'$ represents differentiation with respect to $z$), from which we obtain a system of four first-order ordinary differential equations:

$$U_1' = \frac{1}{z}\left[\frac{4}{\xi_0 + z^4}U_2 - 3g\right] \tag{D 3}$$

$$U_2' = \frac{1}{z}\left[4(\xi_0 + z^4)U_3 + U_2\right] \tag{D 4}$$

$$U_3' = \frac{1}{z}\left[\frac{4}{(\xi_0 + z^4)U_1^3}U_4 + 5U_3\right] \tag{D 5}$$

$$U_4' = 4\alpha(\xi_0 + z^4)z^6 U_1 - 4\beta(\xi_0 + z^4)z^2 U_2. \tag{D 6}$$

The last of these comes from equation (2.10).

The boundary conditions follow from the analysis of the far-field and touch-down behaviour discussed in appendices B and C.3, respectively. In particular, we found that for the far-field behaviour there are two growing modes as $\xi \to \infty$ (or, equivalently, as $z \to \infty$). To eliminate these modes, it is appropriate to impose two boundary conditions that are consistent with the far-field behaviour. We can impose, for instance, the conditions

$$U_2 \sim \frac{\alpha}{\beta}z^4 U_1, \quad U_3 \sim \frac{\alpha^2}{\beta^2}U_1 \quad \text{as} \quad z \to \infty. \tag{D 7}$$

Note that in practice these conditions are imposed at $z = L$ for sufficiently large $L$.

The generic touch-down behaviour has one growing mode as $\xi \to \xi_0^+$ (or, equivalently, as $z \to 0$). To eliminate this mode, it is appropriate to impose one boundary condition, e.g.

$$U_2 = \frac{3\xi_0 U_1}{4} \qquad \text{at} \qquad z = 0, \tag{D 8}$$

which follows from substituting $z = 0$ in the definition of $U_2$ in (D 2).

In addition, to eliminate scale invariance of the solutions, we need to impose one more condition. We can, for example, impose the condition

$$U_1 \sim a_1 z^{4\alpha/\beta - 3} \tag{D 9}$$

with a given value of $a_1$. In our calculations, we use $a_1 = 1$ for direct comparison with figure 3.

This completes the formulation of the boundary-value problem. One of the parameters can be used as the continuation parameter to obtain families of solutions. For example,
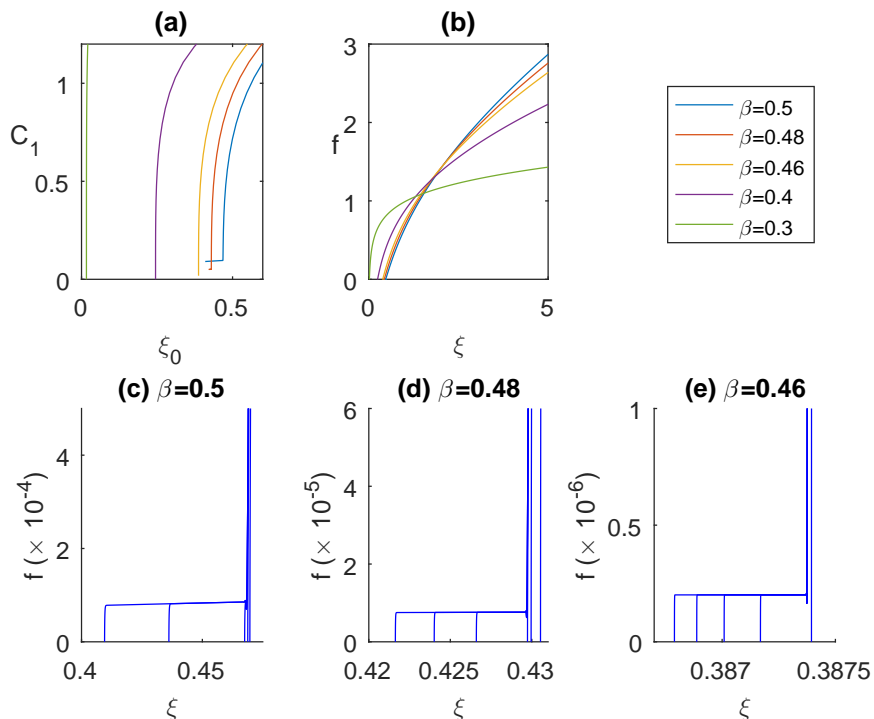
FIGURE 17. (a) Families of self-similar solutions to (2.10) in the $(\xi_0, c_1)$-plane computed using numerical continuation, for various values of $\beta$. As $c_1$ is decreased, the profiles tend to a non-generic profile, shown in (b), with a foot of width $f_{\mathrm{pw}}(\beta)$. (c–e) the region near the apparent contact line for $\beta = 0.5, 0.48, 0.46$, showing the development of the foot as $c_1$ is decreased.

rather than varying a far-field parameter (as is necessary in shooting), we may instead vary $\xi_0$ (for fixed values of $\beta$ and $L$). To track how coefficient $c_1$ varies along a family of solutions, we can add $c_1$ as an additional parameter in the formulation of the boundary-value problem and impose one more boundary condition, e.g.

$$U_1 = c_1. \tag{D 10}$$

We plot the results of continuation in figure 17 in the $(\xi_0, c_1)$ plane for various values of $\beta$. We used $L = 16$ in the computations. Note that for each $\beta > 0$, an apparent critical value of $\xi_0$ is approached as $c_1 \to 0$, until a sharp turn in the $(\xi_0, c_1)$ curve that corresponds to the growth of a 'foot' with a well defined thickness $f_{\mathrm{pw}}$. The apparent contact line location remains fixed as $\xi_0 \to 0$. We may thus build up a $f_{\mathrm{pw}}$ vs $\beta$ curve, that matches with the results from shooting in figure 4. As $\beta$ becomes close to 0.4, the prewetting thickness becomes too small to resolve.

## Appendix E. Numerical scheme

We use a finite-difference scheme to solve the partial differential equation (2.5), subject to appropriate boundary conditions (2.7) and initial condition (2.6) on the domain $[0, 10]$. We first rewrite (2.5) as

$$\frac{\partial h}{\partial t} + \frac{1}{r} \frac{\partial}{\partial r} (rhv) = 0, \tag{E 1}$$

where

$$v \equiv h^2 \frac{\partial \kappa}{\partial r}, \text{ and } \kappa \equiv \frac{1}{r} \frac{\partial}{\partial r} \left( r \frac{\partial h}{\partial r} \right). \tag{E 2}$$

Equation (E 1) can be rearranged in the form

$$\frac{\partial (rh)}{\partial t} + v \frac{\partial (rh)}{\partial r} + rh \frac{\partial v}{\partial r} = 0, \tag{E 3}$$

and we note that the first two terms represent the convection of $rh$ with velocity $v$.

In the healing process, we expect a front advancing towards the origin, and we impose an upwind scheme to discretize the $r$ derivative of $rh$. Hence, if we discretize $h$ at time $t$ by a set of values $\{h_i^t\}_{i=1}^N$ at the nodes $\{r_i\}_{i=1}^N$, we obtain the discretized equation

$$\frac{h_i^{t+\Delta t} - h_i^t}{\Delta t} = -\frac{v_i^t}{r_i} \frac{r_{i+1} h_{i+1}^t - r_i h_i^t}{r_{i+1} - r_i} - h_i^t \frac{v_{i+1/2}^t - v_{i-1/2}^t}{(r_{i+1} - r_{i-1})/2}, \tag{E 4}$$

where

$$v_i^t = \left( h_i^t \right)^2 \frac{\kappa_{i+1}^t - \kappa_{i-1}^t}{r_{i+1} - r_{i-1}}, \tag{E 5a}$$

$$v_{i+\frac{1}{2}}^t = \left( \frac{h_{i+1}^t + h_i^t}{2} \right)^2 \frac{\kappa_{i+1}^t - \kappa_i^t}{r_{i+1} - r_i}, \tag{E 5b}$$

$$\kappa_i^t = \frac{2}{r_{i+1} - r_{i-1}} \left( \frac{h_{i+1}^t - h_i^t}{r_{i+1} - r_i} - \frac{h_i^t - h_{i-1}^t}{r_i - r_{i-1}} \right) + \frac{1}{r_i} \frac{h_{i+1}^t - h_{i-1}^t}{r_{i+1} - r_{i-1}}. \tag{E 5c}$$

The discretized curvature $\kappa_i^t$ is approximated using the central difference of $h_i^t$. In order to resolve the structure of the profiles near the apparent contact line, the code is adaptive and introduces finer meshes in the regions where more nodes are needed. For example, the grid size is in the order of $10^{-5}$ to $10^{-7}$ close to the centre of the hole, and the time step starts from $10^{-18}$, for example, and gradually increases as time progresses. We performed convergence tests to verify that the results are insensitive to further mesh refinements.

## REFERENCES

BACKHOLM, M., BENZAQUEN, M., SALEZ, T., RAPHAEL, E. & DALNOKI-VERESS, K. 2014 Capillary leveling of a cylindrical hole in a viscous film. *Soft Matter* **10**, 2550–2558.

BANKOFF, S. G., JOHNSON, M. F. G., MIKSIS, M. J., SCHLUTER, R. A. & LÓPEZ, P. G. 2003 Dynamics of a dry spot. *J. Fluid Mech.* **486**, 239–259.

BARENBLATT, G. I. 1979 *Similarity, Self-Similarity, and Intermediate Asymptotics*. Consultants Bureau.

BENDER, C. M. & ORSZAG, S. 1978 *Advanced Mathematical Methods for Scientists and Engineers*. McGraw-Hill.

BERTOZZI, A. L., BRENNER, M. P., DUPONT, T. F. & KADANOFF, L. P. 1994 Trends and perspectives in applied mathematics. In *Applied Mathematical Sciences*, pp. 155–208. Springer-Verlag.

BISCHOFBERGER, I., RAMACHANDRAN, R. & NAGEL, S. R. 2014 Fingering versus stability in the limit of zero interfacial tension. *Nat. Commun.* **5**, 5265.

BLOSSEY, R. 2003 Self-cleaning surfaces: virtual realities. *Nat. Mat.* **2**, 301–306.

BONN, D., EGGERS, J., INDEKEU, J., MEUNIER, J. & ROLLEY, E. 2009 Wetting and spreading. *Rev. Mod. Phys.* **81**, 739–805.

BOSTWICK, J. B., DIJKSMAN, J. A. & SHEARER, M. 2017 Wetting dynamics of a collapsing fluid hole. *Phys. Rev. Fluids* **2**, 014006.

BRENNER, M. P., LISTER, J. R. & STONE, H. A. 1996 Pinching threads, singularities and the number 0.0304. *Phys. Fluids* **8**, 2827–2836.

BRETHERTON, F. P. 1961 The motion of long bubbles in a tube. *J. Fluid Mech.* **10**, 166–188.

CRASTER, R. V. & MATAR, O. K. 2009 Dynamics and stability of thin liquid films. *Rev. Mod. Phys.* **81**, 1131–1198.

DALLASTON, M. C., ZHENG, Z., TSELUIKO, D., FONTELOS, M. A. & KALLIADASIS, S. 2017 Self-similar finite-time singularity formation in degenerate parabolic equations arising in thin-film flows. *Nonlinearity* **30**, 2647–2666.

DIEZ, J. A., GRATTON, R. & GRATTON, J. 1992 Self-similar solution of the second kind for a convergent viscous gravity current. *Phys. Fluids A* **6**, 1148–1155.

DIJKSMAN, J. A., MUKHOPADHYAY, S., GAEBLER, C., WITELSKI, T. P. & BEHRINGER, R. P. 2015 Obtaining self-similar scalings in focusing flows. *Phys. Rev. E* **92**, 043016.

DOEDEL, E. J., CHAMPNEYS, R., DERCOLE, F., FAIRGRIEVE, T. F., KUZNETSOV, YU. A., OLDEMAN, B., PAFFENROTH, R. C., SANDSTEDE, B., WANG, X. J. & ZHANG, C. H. 2007 Auto-07p. *Montreal Concordia University* http://indy.cs.concordia.ca/auto/.

DUFFY, B. R. & WILSON, S. K. 1996 A third-order differential equation arising in thin-film flows and relevant to Tanners law. *Appl. Math. Lett.* **10**, 63–68.

EGGERS, J. 1993 Universal pinching of 3D axisymmetric free surface flow. *Phys. Rev. Lett.* **71**, 3458–3460.

EGGERS, J. 2004 Toward a description of contact line motion at higher capillary numbers. *Phys. Fluids* **16**, 3491–3494.

EGGERS, J. & FONTELOS, M. A. 2009 The role of self-similarity in singularities of partial differential equations. *Nonlinearity* **22**, R1–R44.

EGGERS, J. & FONTELOS, M. A. 2015 *Singularities: Formation, Structure, and Propagation*. Cambridge University Press.

FENG, J., ROCHE, M., VIGOLO, D., ARNAUDOV, L.N., STOYANOV, S. D., TSUTSUMANOVA, G. G. & STONE, H. A. 2014 Nanoemulsions obtained via bubble-bursting at a compound interface. *Nat. Phys.* **10**, 606–612.

DE GENNES, P. G., HUA, X. & LEVINSON, P. 1990 Dynamics of wetting: local contact angle. *J. Fluid Mech.* **212**, 55–63.

GRATTON, J. & MINOTTI, F. 1990 Self-similar viscous gravity currents: phase plane formalism. *J. Fluid Mech.* **210**, 155–182.

HERMINGHAUS, S., BRINKMANN, M. & SEEMANN, R. 2008 Wetting and dewetting of complex surface geometries. *Annu. Rev. Mater. Sci.* **38**, 101–121.

HOCKING, L. M. 1983 The spreading of a thin drop by gravity and capillarity. *Q. J. Mech. Appl. Math.* **36** (Feb), 55–69.

HUPPERT, H. E. & WOODS, A. W. 1995 Gravity driven flows in porous layers. *J. Fluid Mech.* **292**, 55–69.

JENSEN, O. E. 1994 Self-similar, surfactant-driven flows. *Phys. Fluids* **6**, 1084–1094.

KALLIADASIS, S., BIELARZ, C. & HOMSY, G. M. 2000 Steady free-surface thin film flows over topography. *Phys. Fluids* **12**, 1889–1898.

KATAOKA, D. E. & TROIAN, S. M. 1997 A theoretical study of instabilities at the advancing front of thermally driven coating films. *J. Colloid Interface Sci.* **192**, 350–362.

LANDAU, L. & LEVICH, B. 1942 Dragging of a liquid by a moving plate. *Acta Physicochim. URSS* **17**, 42–54.

LEVY, R. & SHEARER, M. 2004 Comparison of two dynamic contact line models for driven thin liquid films. *Eur. J. Appl. Math.* **15**, 625–642.

LISTER, J. R. & KERR, R. C. 1989 The propagation of two-dimensional and axisymmetric viscous gravity currents at a fluid interface. *J. Fluid Mech.* **203**, 215–249.

LISTER, J. R. & STONE, H. A. 1998 Capillary breakup of a viscous thread surrounded by another viscous fluid. *Phys. Fluids* **11**, 2758–2764.

LÓPEZ, P. G., MIKSIS, M. J. & BANKOFF, S. G. 2001 Stability and evolution of a dry spot. *Phys. Fluids* **13**, 1601–1614.

McGRAW, J. D., SALEZ, T., BAUMCHEN, O., RAPHAEL, E. & DALNOKI-VERESS, K. 2012 Self-similarity and energy dissipation in stepped polymer films. *Phys. Rev. Lett.* **109**, 128303.

MORIARTY, J. A. & SCHWARTZ, L. W. 1993 Dynamic considerations in the closing and opening of holes in thin liquid films. *J. Colloid Interf. Sci.* **161**, 335–342.

Myers, T. G. 1998 Thin films with high surface tension. *SIAM Rev.* **40**, 441–462.

Oron, A., Davis, S. H. & Bankoff, S. G. 1997 Long-scale evolution of thin liquid films. *Rev. Mod. Phys.* **69**, 931–980.

Padday, J. F. 1971 The profile of axially symmetric menisci. *Phil. Trans. R. Soc. A* **269**, 265–293.

Papageorgiou, D. T. 1995 On the breakup of viscous liquid threads. *Phys. Fluids* **7**, 1529–1544.

Savva, N. & Kalliadasis, S. 2009 Two-dimensional droplet spreading over topographical substrates. *Phys. Fluids* **21**, 092102.

Savva, N. & Kalliadasis, S. 2011 Dynamics of moving contact lines: A comparison between slip and precursor film models. *Europhys. Lett.* **94**, 64004.

Sharma, A. & Ruckenstein, E. 1990 Energetic criteria for the breakup of liquid films on nonwetting solid surfaces. *J. Colloid Interf. Sci.* **137**, 433–445.

Snoeijer, J. H. & Andreotti, B. 2013 Moving contact lines: scales, regimes, and dynamical transitions. *Annu. Rev. Fluid Mech.* **45**, 269–292.

Stone, H. A. & Duprat, C. 2016 CHAPTER 2. low-reynolds-number flows. In *RSC Soft Matter Series*, pp. 25–77. Royal Society of Chemistry (RSC).

Tanner, L. H. 1979 The spreading of silicone oil drops on horizontal surfaces. *J. Phys. D: Appl. Phys.* **12**, 1473–1485.

Taylor, G. I. & Michael, D. H. 1973 On making holes in a sheet of fluid. *J. Fluid Mech.* **58**, 625–639.

Tseluiko, D., Baxter, J. & Thiele, U. 2013 A homotopy continuation approach for analysing finite-time singularities in thin liquid films. *IMA J. Appl. Math.* **78**, 762–776.

Voinov, O. V. 1976 Hydrodynamics of wetting. *Fluid Dyn.* **11**, 714–721.

Witelski, T. P. & Bernoff, A. J. 1999 Stability of self-similar solutions for van der Waals driven thin film rupture. *Phys. Fluids* **11**, 2443–2445.

Yatshyshin, P., Parry, A.O. & Kalliadasis, S. 2016 Complete prewetting. *J. Phys.: Condens. Matter* **28**, 275001.

Yatsyshin, P., Savva, N. & Kalliadasis, S. 2015 Wetting of prototypical one- and two-dimensional systems: Thermodynamics and density functional theory. *J. Chem. Phys.* **142**, 034708.

Zhang, W. W. & Lister, J. R. 1999 Similarity solutions for van der Waals rupture of a thin film on a solid substrate. *Phys. Fluids* **9**, 2454–2462.

Zheng, Z., Christov, I. C. & Stone, H. A. 2014 Influence of heterogeneity on second-kind self-similar solutions for viscous gravity currents. *J. Fluid Mech.* **747**, 218–246.

Zheng, Z., Shin, S. & Stone, H. A. 2015 Converging gravity currents over a permeable substrate. *J. Fluid Mech.* **778**, 669–690.